Deciphering microstructure-defect-property relationships of vacuum-sintered binder jetted fine 316L austenitic stainless steel powder

Mohammad Jamalkhani [a], Mohammadreza Asherloo [a], Omer Gurlekce [a,b], I-Ting Ho [a], Mike Heim [c], Dave Nelson [c], Amir Mostafaei [a,*]

[a] Department of Mechanical, Materials, and Aerospace Engineering, Illinois Institute of Technology, 10 W 32nd Street, Chicago, IL 60616, USA
[b] JSW Steel, 1500 Commercial Ave, Mingo Junction, OH 43938, USA
[c] Nel Pretech Corporation, 8420 183rd Place, Tinley Park, IL 60487, USA

[*] Corresponding author: A. Mostafaei

Email: mostafaei@iit.edu

Abstract

Austenitic 316L stainless steel (SS) powder with a mean particle size of 10.7 μm was binder jetted followed by vacuum sintering to study microstructure-defect-property relationships. It was demonstrated that supersolidus liquid phase sintering (SLPS) facilitated densification to attain a final relative density of 99.4% at 1400 °C for 2 h. Surface topology analysis revealed an average surface roughness of 1.0 μm and a trace number of open-to-surface pores in agreement with the apparent Archimedes density values. Microstructure analysis of the samples sintered at temperatures ≥1370 °C displayed the formation of equiaxed austenitic grains with a mean size of ~33 μm in which δ-ferrite (eutectic phase enriched in Cr and Mo) and σ (intermetallic compound of Fe-Cr-Mo) phases formed at the grain boundaries. Anisotropy shrinkage was seen with a maximum linear shrinkage of 18.4%, 17.7%, and 21.5% in *X*-, *Y*-, and *Z*-directions, respectively. Mechanical testing results showed a yield strength of 202 MPa, tensile strength of 574 MPa, elongation of 90%, and microhardness of 132 $HV_{0.5}$ at the optimum sintering temperature of 1400 °C. Eventually, fractography revealed a brittle-ductile fracture when porosity was more than 10% (sintered at <1370 °C) while a failure containing a combination of deep dimples (sintered at 1400 °C) as well as secondary central cracks and parabolic dimples (sintered at 1430 °C, due to a high shear fracture) was detected in the sintered parts that possess densities above 99%.

Keywords: Additive manufacturing; Densification; Porosity; computed tomography; Mechanical properties; Work hardening.

1. Introduction

As a non-beam-based AM process, binder jetting is a versatile powder bed technique in terms of adaptability in printing various powdered materials, cost-effectiveness, and high production rate. Although this technology brings freedom in manufacturing a wide range of alloys and compounds, parts printed through binder jetting require post-heat treatment (i.e., sintering) to enhance density and properties. Powder characteristics, mainly shape and particle size, affect sintering thermodynamics and kinetics. Densification of a fine powder with a mean size of <25 μm occurs at low sintering temperatures due to higher capillary force of the fine powder.

To date, the research on the binder jetting of the 316L SS powder was based on the exploration of the role of the processing parameters on green part density and understating the densification behavior via sintering and resultant final microstructure and mechanical

performance. Lecis et al. [1] studied the effect of the layer thickness and binder saturation on the green density of the binder jetted fine 316L SS powder (<-22 μm). Although binder saturation (55% or 70%) had a minimal impact on the green density, the increase of layer thickness led to reduction of the green density from 54% to 50%. While higher binder saturation could improve the strength of the as-printed body, it resulted in an increased number of pores and inclusions, thereby decreasing the final density. Batmaz et al. [2] studied the role of the particle size distributions on the green and resultant sintered densities. It was shown when a bimodal fine powder (9-40 μm) was binder jetted, a green density of 58±2% was achieved, and a final density of ~94% was attained by sintering at 1400 °C for 5h. The remnant pore fraction of 6% would be related to the formation of in-layer void during printing. Rios et al. [3,4] showed that the excessive C, H, and N cause by polymer binder was eliminated during the burnout step. In addition, anisotropy in the relative density was observed in the solid area fraction analysis and a relative density between 96% and 99% was reported. Kumar et al. [5] attained a relative density of 94-96% by sintering at 1380 °C for 2 h with a tensile strength of 550 MPa and elongation of 80%. Chen et al. [6] demonstrated that the initial green density directly affected the shrinkage and final density. Sintering at 1440 °C for 3 h resulted in formation δ-ferrite at the grain boundary in which a final relative density of 98.7% with a maximum tensile strength of ~600 MPa and elongation of ~60% were reported.

Uniform densification of the binder jetted parts remained as a challenging issue in the AM community, and the existing knowledge on the sintering behavior of 316L SS is limited to only specific temperatures, e.g., 1370 °C and 1380 °C, in which 1-2% porosity was reported in the parts. In addition, the quality of parts, mainly internal defects and porosity, has different definitions in various industries. Sintered porous 316L SS with an open-cell structure is being employed in bone-in-growth orthopedic implants [7]. On the other hand, in nuclear industry, 316L SS alloy which is massively used to build several parts of the reactor pressure vessels requires to have a near fully dense structure [8–10]. In order to leverage the applications of 316L SS, it is necessary to fundamentally investigate the correlation between the sintering temperature and grain structure, porosity, and mechanical properties. Here, a systematic study was designed to rationalize the role of sintering temperature on the microstructure-defect-property relationship.

2. Materials and experiments

2.1. Feedstock powder

Gas-atomized 316L SS alloy (d_{90} = 22 μm) was supplied by Sandvik Osprey Company with the chemical composition given in Table 1. Particle size distribution (PSD) was found to be d_{10} = 3.3 μm, d_{50} = 10.7 μm, d_{90} = 19.6 μm using LS13 320 XR System, confirmed by the captured scanning electron microscope images (SEM JEOL 5900LV) shown in Figure 1 (A). It was seen that the majority of 316L SS powders had spherical morphology with a circularity of 90% [1]. As shown in Figure 1 (B) thermogravimetric analysis (TGA) and differential scanning calorimetry (DSC) were implemented by a Setaram setsys 16 on the virgin 316L SS powder using temperature scans from 25−1480 °C with a heating rate of 5 °C/min in Argon atmosphere. In the endothermic peak of the DSC test, a phase transformation was observed in which a major shift occurred in the flow curve at a

temperature close to 1433 ℃, considered as the solidus temperature of the virgin 316L SS powder.

Table 1. The chemical composition (% wt.) of 316L SS, supplied by Sandvik Osprey Company compared with the nominal composition.

	Fe	C	Si	Mn	P	S	Cr	Ni	Mo
Nominal composition	Bal.	≤0.030	≤1	≤2	≤0.045	≤0.030	16–18	10–14	2–3
Manufacturer	Bal.	0.03	0.58	2.19	--	--	18.28	10.9	2.12

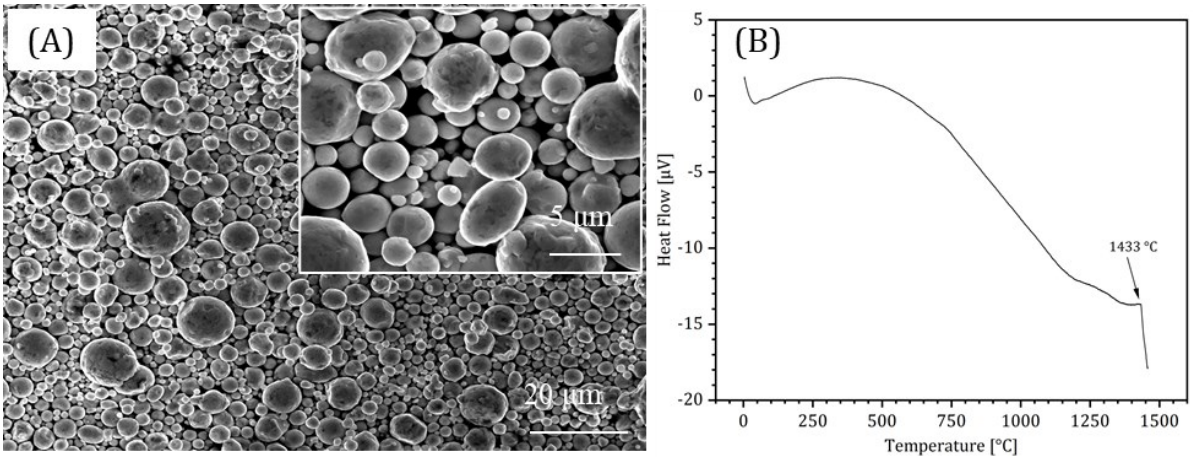

Figure 1. (A) Scanning electron micrographs of 316L SS powder at two different magnifications and (B) differential scanning calorimetry (DSC) and thermogravimetric analysis (TGA) of 316L SS powder.

2.2. Binder jetting of 316L SS powder

The optimum binder jetting process parameters are given in Table 2. An AquaFuse water-based binder (BA-005 solution provided by the ExOne Company) was used composed of ethylene glycol monobutyl ether with 10 vol% and ethylene glycol with 20 vol%. Since fine powders have a high tendency to absorb moisture, the feedstock was dried prior to the binder jetting process at 185 °C for 8 h (drying powder) and then was sieved by 106 µm mesh to enhance uniform sieving and spreading of powder on the bed.

Table 2. Specified optimum process parameter inputs for ExOne Innovent+ binder jetting system.

Printing process parameters	**Optimum set values**
Layer thickness (µm)	50
Recoat speed (mm/s)	40
Smoothing roller speed (rpm)	600
Roughing roller speed (rpm)	300
Roller traverse speed (mm/s)	3
Intensity of ultrasound vibrator (%)	100
Binder saturation (%)	80
Binder set time (s)	8
Drying time (s)	10
Bed temperature (°C)	40
Emitter output (%)	100

To study the sintering behavior and microstructure evolution, cubes with dimensions of 15 mm × 20 mm × 10 mm (*XYZ* dimensions) were fabricated using an Innovent+ binder jet printer (ExOne Company) with a 30 pL print head. As-printed parts with a relative density of 53.6±0.6% was attained. Dog bone specimens were designed in accordance with the ASTM

standard E8/E8M and printed horizontally (y-oriented) on the powder bed for mechanical testing.

2.3. Curing and sintering steps

Curing was conducted in an oven at 185±2 °C for 8 h in an air atmosphere. Then, binder jetted parts were depowdered to remove loose powders. The cured samples were placed in an alumina crucible and sintered in a tube furnace (Across International FT1700) under vacuum (vacuum level was $\sim 10^{-5}$ bar). To minimize potential oxidation of the 316L SS powder, a titanium sponge, also known as an oxygen getter, was placed inside the crucible. The binder burnout step (*a.k.a.* debinding) was performed at 600 °C with a dwell time of 1 h. Parts were sintered at different temperatures ranging between 1220 °C and 1430 °C and a holding time of 2 h with a heating rate of 5 °C/min. For each sintering condition, three samples were sintered simultaneously to consider the repeatability of the densification study.

2.4. Characterizations

Relative density of the sintered samples was determined based upon the Archimedes' method (ASTM B962-17) and solid volume fraction approach. From Archimedes' principle, two relative density values comprising bulk density and apparent density are obtained [11]. Cubes were immersed in the distilled water for 24 h under a vacuum atmosphere, and mass measurements were implemented by a Sartorius precision balance with 0.01 mg accuracy.

The solid area fraction is another criterion for assessing the relative bulk density of the sintered alloy based on the 2D image analysis. For this purpose, sintered cubes were sliced parallel to the build direction on the XZ face using a wire electric discharge machine (Mitsubishi FX10k Wire-EDM machine). The sliced parts were hot-mounted using MetLab phenolic thermosetting molding powder. Then, the mounted samples were ground (using SiC sandpapers up to P4000) and polished with 3 μm diamond abrasive, 1 and 0.05 μm Al_2O_3 abrasive, reaching a final polishing step of 0.04 μm colloidal silica by implementing a platen grinder-polisher machine (Buehler Phoenix 4000). A Keyence VHX-7100 digital microscope was used for optical microscopic observations, porosity analysis, and surface topology of the as-printed and sintered specimens.

The linear shrinkage measurements were carried out in three orthogonal directions based on the directional difference after densification. Porosity measurements and counts were performed on the original optical micrographs with the "automatic area measurement" feature in the Keyence VHX-7100 digital microscope software. To examine the spatial distribution of pores in a unit volume of the as-printed part, a ZEISS Metrotom 800 X-ray micro-computed tomography (μ-CT) scanner was utilized at the energy and current of 130 kV and 30 mA featuring an Al 2.0mm filter, averaging frames of 4, and angular range of 360° with a step size of 0.12° resulting in a spatial resolution of 5.1 μm/pixel. Collected data was then reconstructed and analyzed using Volume Graphics Studio Max 3.5.1.

Microstructural observations of the sintered parts (mainly grain analysis) were conducted by employing an SEM microscope (JEOL 5900LV) equipped with an Oxford Instruments electron backscatter diffraction (EBSD) detector operating at an acceleration voltage of 20 keV and step size of 0.75 μm. EBSD data was processed using MTEX, a free MATLAB-based toolbox [12]. X-ray diffraction pattern analysis (XRD) was performed on samples' curved surfaces using an x-ray diffractometer (model Thermo ARL) with Cu-Kα

radiation (λ = 1.5406 Å, 35 kV and 30 mA), a 2θ ranging between 30-100º, a scan speed of 1 s/step, and scan step of 0.02 º at an ambient temperature. Carbon (C), oxygen (O), nitrogen (N), and sulfur (S) contents of the virgin powder, binder jetted and cured parts, and sintered samples at selected temperatures were measured using LECO (models TCH600 and CS744).

Tensile tests were conducted to determine the yield strength, ultimate tensile strength, and elongation using an MTS 880 machine at a controlled rate of 0.03 in/min on the as-sintered specimens at selected sintering temperatures. Fractography was then followed on the tensile specimens using an optical microscope and field emission scanning electron microscope (FESEM, model JEOL JSM-6701F) equipped with energy dispersive spectroscopy (EDS). Also, the hardness was measured using a Vickers microhardness tester (Buehler model Micromet 2) at a load of 500 gf and dwell time of 15 s. To study the effect of work hardening on grain evolution, a vertical section was prepared on the mechanical testing sample (sintered at 1400 °C), then microhardness and texture analysis were carried out. Spatial distribution of pores was also assessed on one side of the failed tensile specimen using optical microscopy and μ-CT analysis.

3. Results and discussion

3.1. Porosity, relative density, and shrinkage measurements

Figure 2 showed μ-CT results in 3D and 2D shadow projection from the as-printed and cured binder jetted sample. The *YZ* plane, in which layers with uniform thickness were visible, indicated a layer-by-layer binder jetted metal powder. On the *XZ* plane, the layer-wise binder jetting deposition was not as visible as in the *YZ* plane; however, after the porosity analysis, pores between the layers were easily identified. On the *XY* plane, a periodic variation in density within the layer plane was seen which was related to the ballistic ejection of fine powder hit by a liquid binder. The visibility of these density variations in the build directions (*XZ* and *YZ* planes) and the layer plane (*XY* plane) of the binder jet part are evidence of how part quality impacts densification behavior and shrinkage. Similar observations were reported in [13–15].

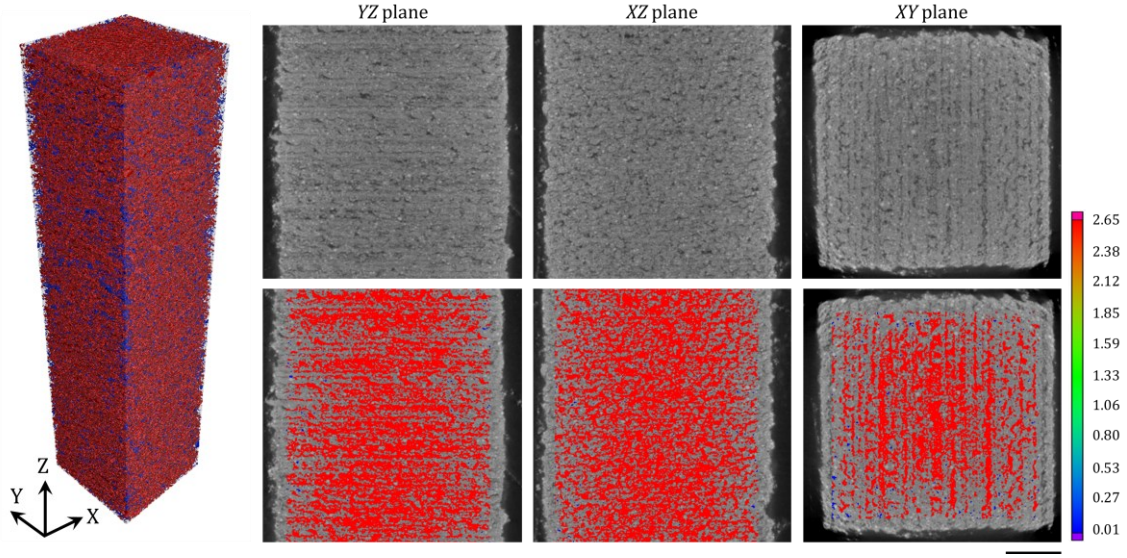

Figure 2. μ-CT results illustrating 3D and 2D shadow projection of the as-printed and cured binder jetted 316L SS part. The color bar showed the equivalent pore diameter in mm. The scale bar is 500 µm. The dimension of the μ-CT sample was 2×2×10 mm^3.

Figure 3 demonstrated the evolution of the porosity for the binder jetted 316L SS powder vacuum-sintered at temperatures ranging from 1220 to 1430 °C with a holding time of 2 h. At the sintering temperature of 1220 °C, the size and shape of the pores are dominantly large and irregular with a small fraction of small and round ones. The obtained relative density based on the solid area fraction measurements at the sintering temperature of 1220 °C was ~84.0±1.1%. When the sintering temperature increased to 1250 °C, the solid area fraction slightly increased, and the population of large, irregular pores diminished while number of small-sized, spherical pores enhanced. This would be attributed to the neck growth at the powder-powder interface, and subsequently pore isolation which resulted in the formation of dominant small-sized pores in the microstructure [11]. By the increase of the sintering temperature to 1325 °C, the majority of such spherical, small-sized pores were removed from the microstructure because of pore closure as a result of densification. In addition, optical micrographs of the parts sintered at temperatures below 1325 °C revealed inter-layer voids and printing lines related to the ballistic ejection of fine powder hit by liquid binder [16]. In fact, densification at sintering temperatures up to 1325 °C eased neck growth, healed small-sized pores, and also lowered the population of large, irregular pores such that above the sintering temperature of 1340 °C, those inter-layer porosity line disappeared.

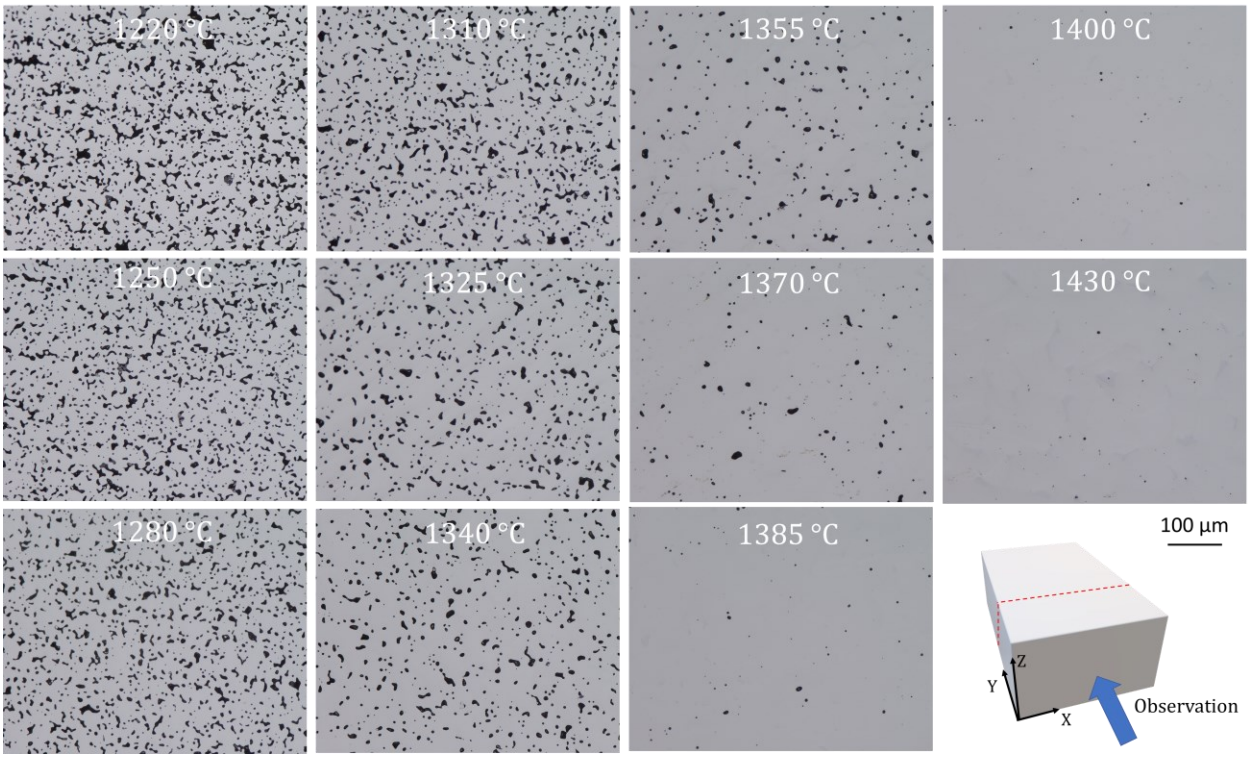

Figure 3. Optical micrographs on the cross-section of the binder jetted 316L SS powder as a function of sintering temperature. The presented cross-sectional micrographs were collected on the *XZ* surface.

Above the sintering temperature of 1355 °C, morphology of the remnant large irregular pores transformed to spherical ones. Then as the sintering temperature increased to 1385 °C, the pore population dramatically decreased and a relative density of ~99% was achieved. Further increase in the sintering temperature promoted pore filling and a maximum relative density of 99.4% was measured at the sintering temperature of 1400 °C. After solidification, δ-ferrite appeared at the grain boundaries which was visible with a gray

color in Figure 3. Phase analysis using SEM equipped with EBSD suggested the presence of δ-ferrite whose details were discussed in section 3.3. Although a few studies [14,17,18] indicated that the excessive C, O, and N contents could be removed during the debinding and sintering, the excessive C content (as contamination on the particle surfaces) could possibly lead to a downshift in the solidus temperature in virgin powder resulting in supersolidus liquid phase sintering (SLPS). Finally, small, spherical pores (i.e., <2.5 μm on 2D micrographs) was seen in the sintered parts at temperatures beyond 1385 °C with a relative density of >99%.

Figure 4 (A) represented relative density of the binder jetted 316L SS at different sintering temperatures ranging from 1220 to 1430 °C derived by Archimedes' principle (relative bulk density and relative apparent density) and solid area fraction method acquired by the 2D image analysis of the micrographs shown in Figure 3. The fraction of the open pores connected to the surface is determined by evaluating the difference between the relative bulk density and relative apparent density obtained via Archimedes' principle. It was noticed that such a difference was about 15% when a specimen was sintered at 1220 °C, and as the temperature reached 1340 °C, the difference declined to <2%. This behavior confirmed that pore closure occurred on the surface with increasing the sintering temperature while there were still a few open-to-surface pores in the structure beyond 1340 °C. As the sintering temperature enhanced to 1400 °C and higher, the majority of the open-to-surface pores were closed (see Figure 6).

In temperatures ranging from 1220 to 1310 °C, the change in the relative bulk density is rather gradual in comparison with the temperatures ranging from 1310 to 1355 °C, in which small changes in sintering temperature led to significant shifts in the density values. The latter is known as the "intermediate stage of sintering" in which the part density reaches ~95%. The calculated equilibrium phase fraction (see Figure 5) revealed formation of liquid phase above ~1366 °C which revealed SLPS was locally active. To clarify, this estimation was based on the given chemical composition of virgin including C, O, N, and S content in the sample after burnout step (see Table 1 and Table 3). Thus, sintering at ≥1370 °C was dominated by SLPS (as promoted by a higher carbon content), and densification was in the "final stage of sintering." This stage could also be recognized based on the observed trend in Figure 4 (A) in which the sintering rate became remarkably reduced beyond 1370 °C. When the sintering temperature reached 1400 °C, a relative density of 99.4 ± 0.1 % was achieved. A slight decrease in the relative density was observed in the sintered part at 1430 °C. This behavior could be associated with the higher portion of the formed liquid phase during sintering which contracted during solidification and left fine pores behind [11].

In Figure 4 (B), the linear shrinkage, $\frac{\delta L}{L}$, in three different directions including (1) *X* as the powder recoating axis, (2) *Y* as print head traverse axis, and (3) *Z* as build direction axis was shown against sintering temperatures. Similar to the relative density measurements, the linear shrinkage in all directions increased as the sintering temperature rose; nonetheless, it peaked at 1400 °C and then slightly decreased while the sintering temperature reached 1430 °C. As explained earlier, the slight decrease in the shrinkage beyond 1400 °C could be related to the formation of a large-in-size liquid phase at a sintering temperature of 1430 °C. When parts were cooled down to room temperature, liquid → solid transformation occurred at the grain boundaries, and solid grains hindered free contraction and shrinkage in the part. Accordingly, sintered parts sintered at 1430 °C experienced lower shrinkage level compared with the parts sintered at 1400 °C.

During the sintering process, shrinkage varied in three different directions. At the low sintering temperature of 1220 °C to 1325 °C, anisotropy shrinkage was noticed in *Z* to be ~2-3% and in *X* to be ~1% higher than that in the *Y*-direction. Above 1340 °C, it was seen that the anisotropy shrinkage in *Z* enhanced to 4-5% higher than in the *Y*-direction while the difference in shrinkage between the *X*- and *Y*-directions was unchanged and remained at ~1%. Generally, in-layer porosity forms during the binder jetting process by the binder droplets across the build box; thus, the linear shrinkage in the *Z* axis in all sintering temperatures is noticeably higher than that in the *X* and *Y*-directions. In an effort to investigate the binder jetting process using high-speed synchrotron X-ray imaging, Parab et al. [19] realized that within the interaction of the binder droplets and the powder bed, binder droplets and trailing satellite droplets cause a disturbance in the powder bed resulting in a drift or ejection in the fine powders. Hence, such ballistic drifts in the *X* axis as well as the created interaction depth in the *Z*-direction result in lines of sub-surface porosities. In other words, when several particles are ejected due to binder-powder interactions and the formed gap is not refilled by the subsequent spread layer of fine powder, large pores will appear in the as-printed part [11,16]. Mostafaei et al. [11] explained that these gaps could become obvious after the debinding/burn-out step followed by solid-state sintering at low temperatures.

The normalized number of pores per unit area and circle equivalent diameter of porosities were analyzed against sintering temperature, and results were shown in Figure 4 (C) and Figure 4 (D), respectively. Typically, as the sintering temperature increased, the number of pores per unit area decreased aligned with the qualitative examination on 2D micrographs of Figure 3. Nevertheless, when the sintering temperature increased from 1220 to 1250 °C, an increase in the number of pores per unit area was seen, which could be ascribed to the neck growth and the possible splitting of larger pores into the finer ones. The downward trend of the pore closure in the sintering temperatures ranging from 1250 to 1370 °C was substantial; however, as the sintering temperature increased from 1385 °C to 1430 °C, the number of pores per unit area declined in a more moderate fashion and reached a plateau. This showed that the densification rate is rapid at relatively low sintering temperatures, and then as the sintering temperature reached close to the solidus temperature (i.e., 1366 °C after burnout step), the speed of densification decreased. Since the size of the porosity has a vital role in determining the mechanical properties of the final binder jetted part, the circular equivalent of the pore size on 2D cross-sections of the densified samples was measured, and the results were presented in Figure 4 (D). Generally, the pore size decreased as the sintering temperature increased. In addition, the (standard) deviation was much more intense in the relatively low-temperature sintered parts as there were a mixture of large- and small-sized pores coexisting in the sintered body. Meanwhile, the (standard) deviation and outliers' data of the pore size for the parts sintered at comparatively high temperatures are in a close range of the mean value of the pore size presenting a more uniform pores in terms of sizes and shape. It is noteworthy that these analyses were carried out on the 2D optical micrographs while pore structure in 3D would show a slightly different behavior; thus, X-ray micro-computed tomography could complement these observations.

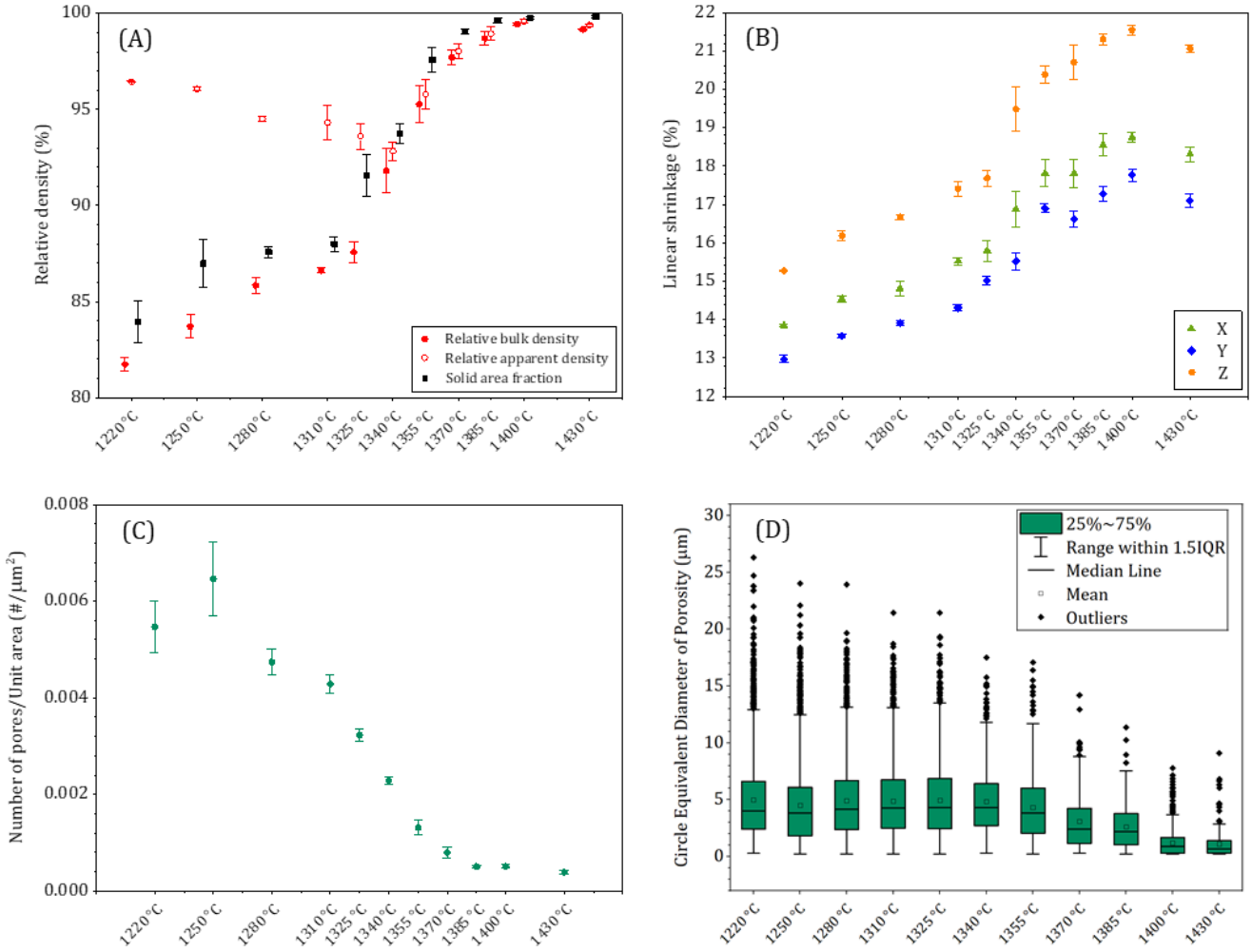

Figure 4. (A) Relative density, (B) shrinkage in *X*-, *Y*-, and *Z*-directions, (C) normalized number of pores, and (D) circle equivalent diameter of porosity for the binder jetted 316L SS powder as a function of sintering condition. In all graphs, the mean and standard deviation are plotted at each sintering condition. In "A", data points of the relative density were staggered for better comprehensibility.

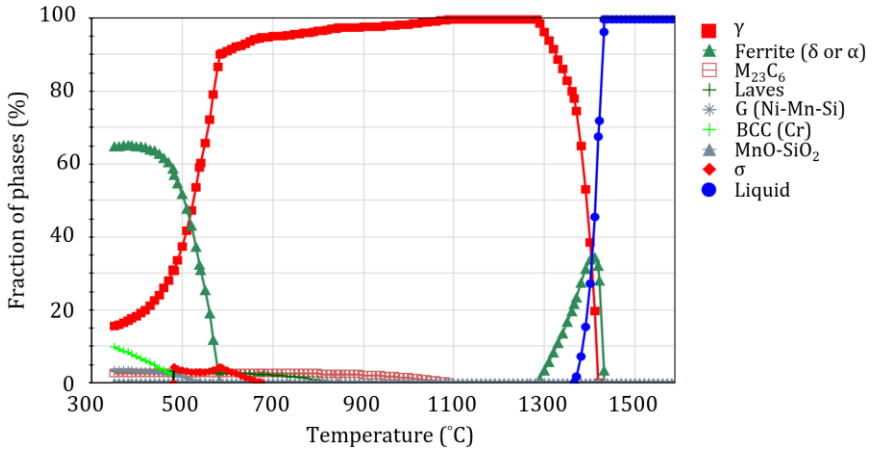

Figure 5. Equilibrium phase evolution for the binder jetted 316L SS alloy after burnout step using JMatPro software. Solidus temperature was found to be at ~1366 °C.

3.2. Surface topology and roughness measurement

Figure 6 illustrated scanning electron micrographs taken from the top surface of the sintered samples. The evolution of surface topology and pore removal as a function of sintering temperature were visible on the surface. The majority of pores were closed at sintering temperatures of 1385 ℃ or higher suggesting potential enhancement of mechanical strength and fatigue performance.

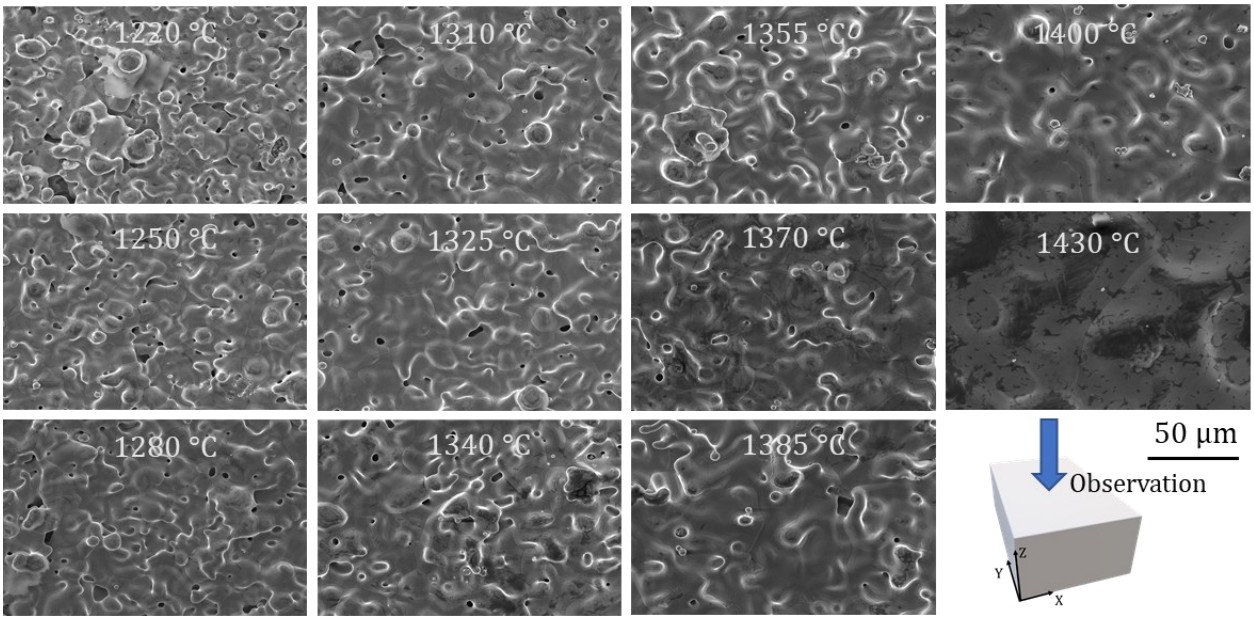

Figure 6. Scanning electron micrographs taken from the top surface of the binder jetted 316L SS specimens as a function of sintering temperature.

Figure 7 displayed optical surface topography profiles of the as-printed and sintered binder jetted 316L SS. The average roughness (R_a) and average maximum peak to valley of five consecutive sampling lengths (R_z) values. Firstly, print lines were visible on the optical surface topography profile of the as-printed part. Even after sintering at 1400 ℃ and 1430 ℃, these lines were seen on the surface The R_a value for the as-printed part was 1.6 µm. Myers et al. [20] showed when the same powder was binder jetted with an Innovent+ printer using different process parameters (e.g., layer thickness, droplet size, spread speed), the average roughness varied between 4 µm and 10 µm. Higher reported values of the roughness might be related to the roller rotation and transverse speed which are needed further optimization in that study. After sintering at 1400 ℃, the average roughness decreased to 1.0 µm, which is much lower than the reported values for coarse metal powder with a PSD of 20-50 µm (e.g., R_a = ~8 µm) [21]. At the maximum sintering temperature of 1430 ℃, it was observed that the roughness increased to 4.0 µm.

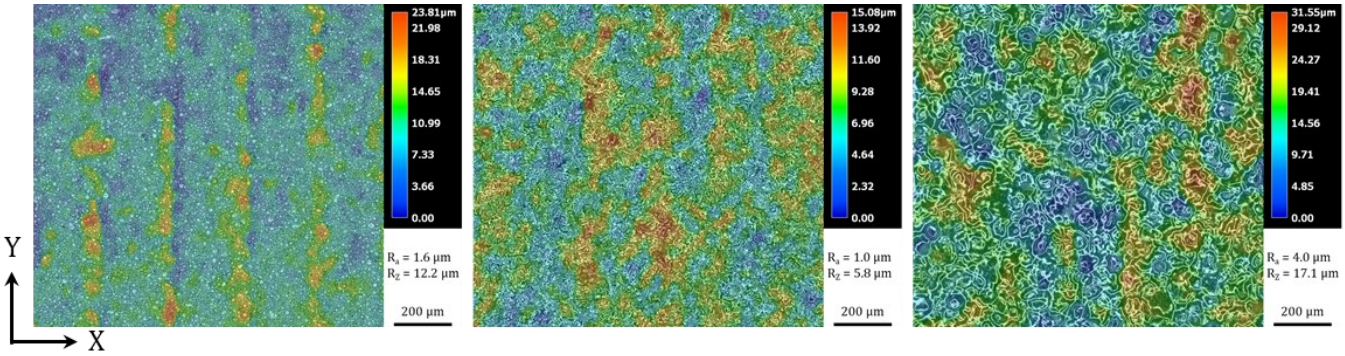

Figure 7. Optical surface topography profiles in (left) as-printed binder jetted part, (middle) sintered at 1400 °C, and (right) sintered at 1430 °C.

3.3. Elemental analysis, microstructure observations, and grain size measurements

Concentration of C, O, N, and S are of high importance regards to sintering mechanism, microstructure evolution, phase formation and mechanical properties. Based on elemental analysis, the C, O, and N content of the virgin powder was 0.025, 0.129, and 0.113 wt%, respectively, which increased to 0.220, 0.272, and 0.156 wt% after binder jetting followed by the curing step. Also, the fraction of these elements altered after burnout step to lower numbers. After sintering above 1340 °C, fraction of these elements was below the original powder. The increase of the three elements after binder jetting was related to the polymer binder in the samples, while the reduction during sintering is caused by binder burn-out and potentially due to decomposition/desorption of C, N and O rich layers existing on the surface of the original particles. In section 3.6., detailed discussion on the role of vacuum sintering on part chemistry is elaborated.

Table 3. Measured carbon, oxygen, nitrogen, and sulfur content of the virgin powder, binder jetted cured part and post heat treated samples at different sintering temperatures in [wt%].

Samples	Carbon	Oxygen	Nitrogen	Sulfur
Virgin 316L SS powder	0.0250	0.1290	0.1130	0.0068
Binder jetted and cured	0.2200	0.2720	0.1560	0.0060
After burnout step at 600 °C for 1 h	0.1350	0.0850	0.0330	0.0056
Sintered at 1250 °C for 2 h	0.0800	0.0248	0.0151	0.0040
Sintered at 1340 °C for 2 h	0.0240	0.0093	0.0022	0.0045
Sintered at 1370 °C for 2 h	0.0270	0.0092	0.0020	0.0054
Sintered at 1400 °C for 2 h	0.0270	0.0072	0.0016	0.0054
Sintered at 1430 °C for 2 h	0.0250	0.0068	0.0012	0.0048

To analyze the microstructure and grain evolution, EBSD analysis was carried out on the samples sintered at temperatures ranging between 1220 °C and 1430 °C. Figure 8 compared grain evolution as a function of sintering temperature at two locations of (1) near the edge and (2) center of the cross-section. Results indicated uniformity of the features (i.e., grain size and pore size) regardless of the sintering temperature. This showed that the sintering condition in terms of heating cycles was well designed and the resultant microstructure was consistent in all applied sintering temperatures. The micro-scale uniformity is crucial in the binder jetted metals to secure the mechanical properties.

The microstructure of the sintered 316L SS was mainly characterized by equiaxed austenitic grains (red color in the phase map) [22] containing annealing twins. In addition, δ-ferrite appeared at the grain boundaries (blue color in the phase map) of the parts sintered at 1370 ℃ and higher temperatures due to liquid phase formation promoted by a higher C content on the powder surfaces [1,23]. Quantitative analysis showed that the fraction of δ-ferrite formed at the grain boundaries was ~1.23±0.03% in the sample sintered at 1370 ℃ and increased to ~2.98±0.09% in the sample sintered at 1430 ℃. Regarding the grain size, a gradual grain growth occurred with increasing sintering temperature from 1220 to 1325 ℃. Afterwards, a significant grain coalescence was seen at the sintering temperatures of 1340 and 1355 ℃ in which bimodal grain size was visible in the EBSD maps; however, not a considerable difference in grain size was observed beyond the sintering temperature of 1355 ℃ in which grain coalescence reached a plateau and grain coarsening rate decreased. By a quantitative comparison of the mean grain size, relative density, and fraction of the δ-ferrite at the grain boundary versus the sintering temperature, it was found that the sintering temperature of 1400 ℃ could provide a considerable high relative density of 99.4$\pm$0.1 % with a mean grain size of ~33 μm and a smaller fraction of liquid phase at the grain boundaries (~2.02$\pm$0.03%) bringing a superior mechanical strength and ductility to the binder jetted 316L SS.

The frequency and cumulative probability distributions of the grain size were plotted for two different locations near the edge and center of the cross-sections, and the results were shown in Figure 9 (A) and Figure 9 (B), respectively. Also, the mean grain size values against sintering temperature were shown in Figure 9 (C). The distribution profile of the grain size showed that at low sintering temperatures, the variance in the grain size is relatively small, and most of the grains are <20 μm. With increasing the sintering temperature, i.e., >1310 ℃, such a variance becomes remarkable because of coexistence of small (<20 μm) and large (20<x<60 μm) grains in the microstructure. At 1355 ℃, sintered parts possessed grains with a mean size of 29.4 μm in which significant grain growth was in effect compared to 1340 ℃ with a mean grain size of 19.6 μm. Above the sintering of 1370 ℃, the relative frequency of grains (see Figure 9(A)) indicated that the larger grains (20<x<60 μm) with a mean grain size of ~33 μm were dominant in the microstructure, and the grain growth proceeded with the increasing sintering temperature at a much lower growth rate. Comparing the quantitative analyses of the EBSD maps of the near the edge and center of the cross-sections (as shown in Figure 9(A,B)), a negligible difference was observed indicating a uniform microstructure throughout the entire samples. A few studies showed anisotropy in the grain size and remnant pore fraction between the center and near the edge sections [4,24–26]. In the current study, homogeneous sintered microstructure was related to the production of as-printed parts with a uniform green density throughout each part as well as uniform thermal cycling during sintering.

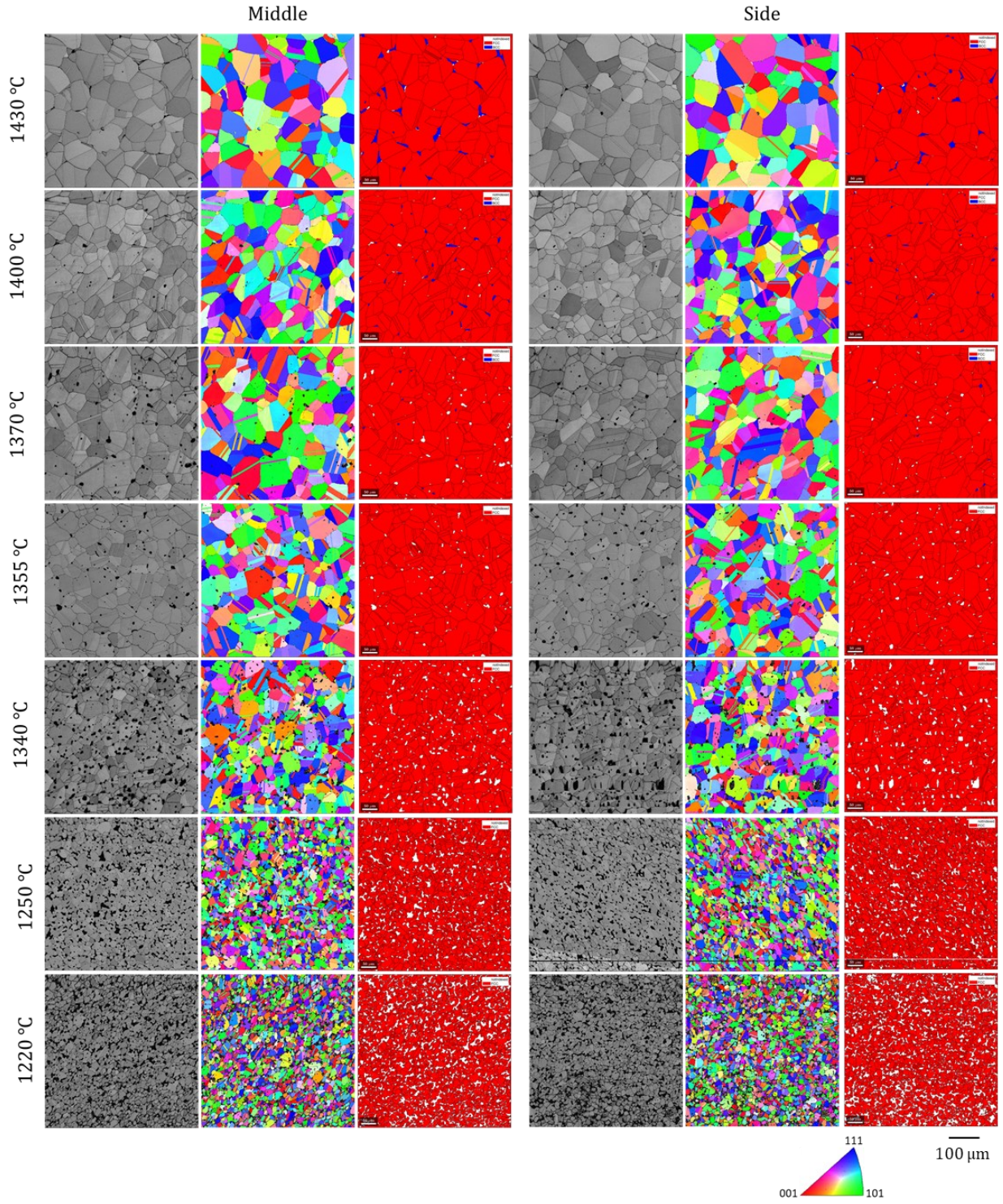

Figure 8. EBSD data: (left) scanning electron micrographs, (middle) inverse pole figure (IPFY), and (right) phase map results collected on the XZ cross-section of the binder jetted 316L SS alloy sintered at temperatures ranging from 1220 to 1430 °C. The scale bar is 100 µm. White areas are unindexed (pores), red areas are austenitic grains, and blue regions at the grain boundaries are δ-ferrite (in samples sintered at ≥1370 °C). Sigma (σ) phase was not shown because the fraction was extremely low and difficult to visualize at low magnifications.

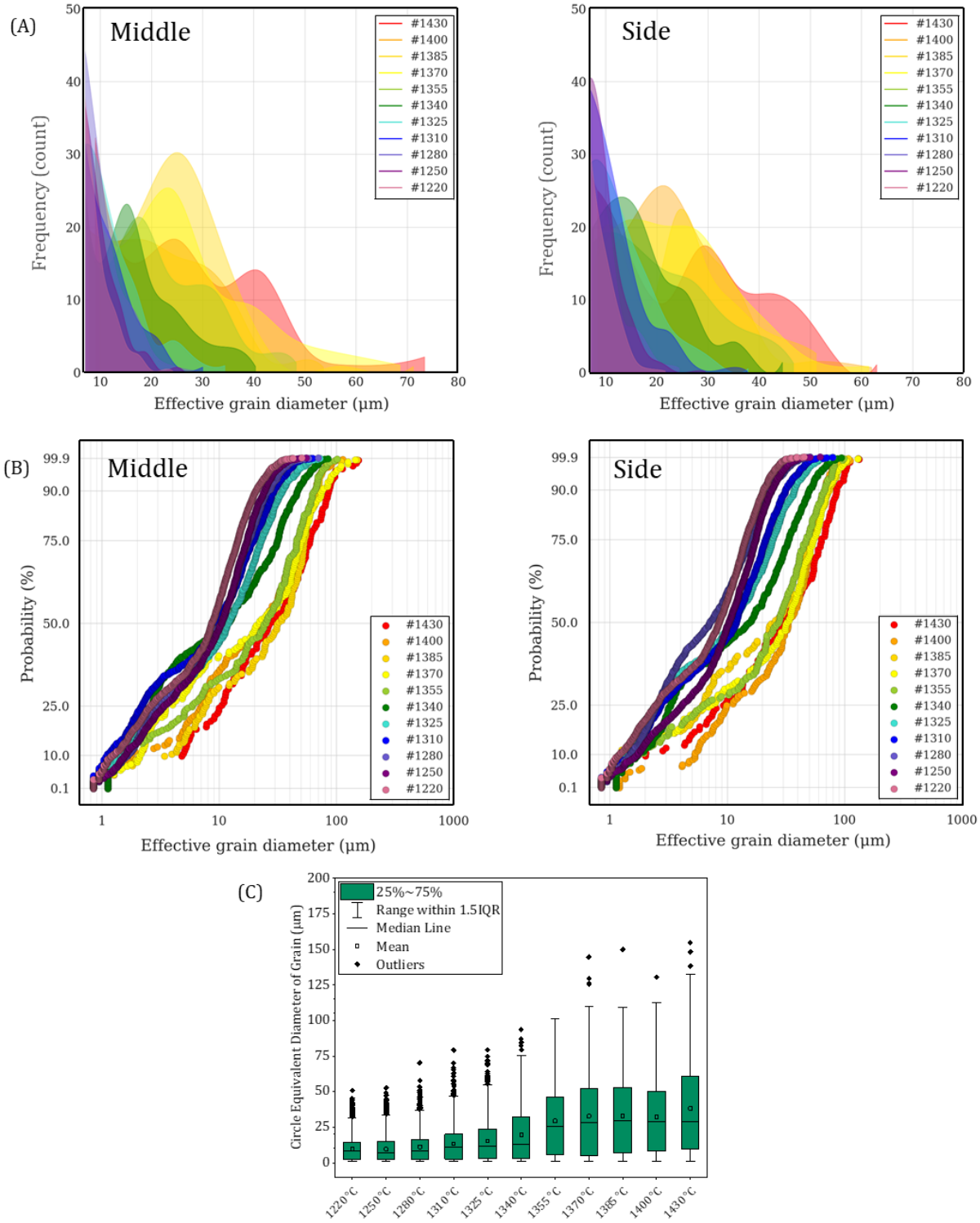

Figure 9. (A) Grain size distribution, (B) cumulative probability distribution of grains, and (C) circle equivalent diameter of the grains at the sintering temperatures ranging from 1220 to 1430 ℃.

Optical and scanning electron micrographs as well as elemental analysis of the sintered sample at 1430 ℃ were shown in Figure 10. Austenitic grains with annealing twins

were obvious in the microstructure (Figure 10(A)). Additionally, the presence of the δ-ferrite phase at the grain boundaries with a higher concentration of Cr and Mo as ferrite stabilizers was confirmed by the elemental analysis as illustrated in Figure 10B-D. The EDS analysis showed that the Ni concentration was ~12.2 wt.% in the matrix while it was only ~5.9% in the δ-ferrite phase. Also, the concentration of Cr and Mo was ~22.3 wt.% and 2.7 wt.% in the δ-ferrite phase (see Table 5). In most cases, Ni is a γ-stabilizer and is present in the γ-austenite matrix while Cr and Mo are in charge of advancing the grain boundary δ-ferrite in 316L SS alloy at relatively high sintering temperatures. These observations were in agreement with recently published articles on the binder jetted 316L SS [1,4,5]. In addition, at sintering temperatures of ≥1370 °C when the fraction of δ-ferrite is more than 2%, there is a possibility of the formation of the sigma (σ) phase (Fe-Cr-Mo intermetallic compound with a tetragonal crystal structure). This σ phase was seen in parts sintered at 1430 °C, in which the fraction of δ-ferrite was about 3%.

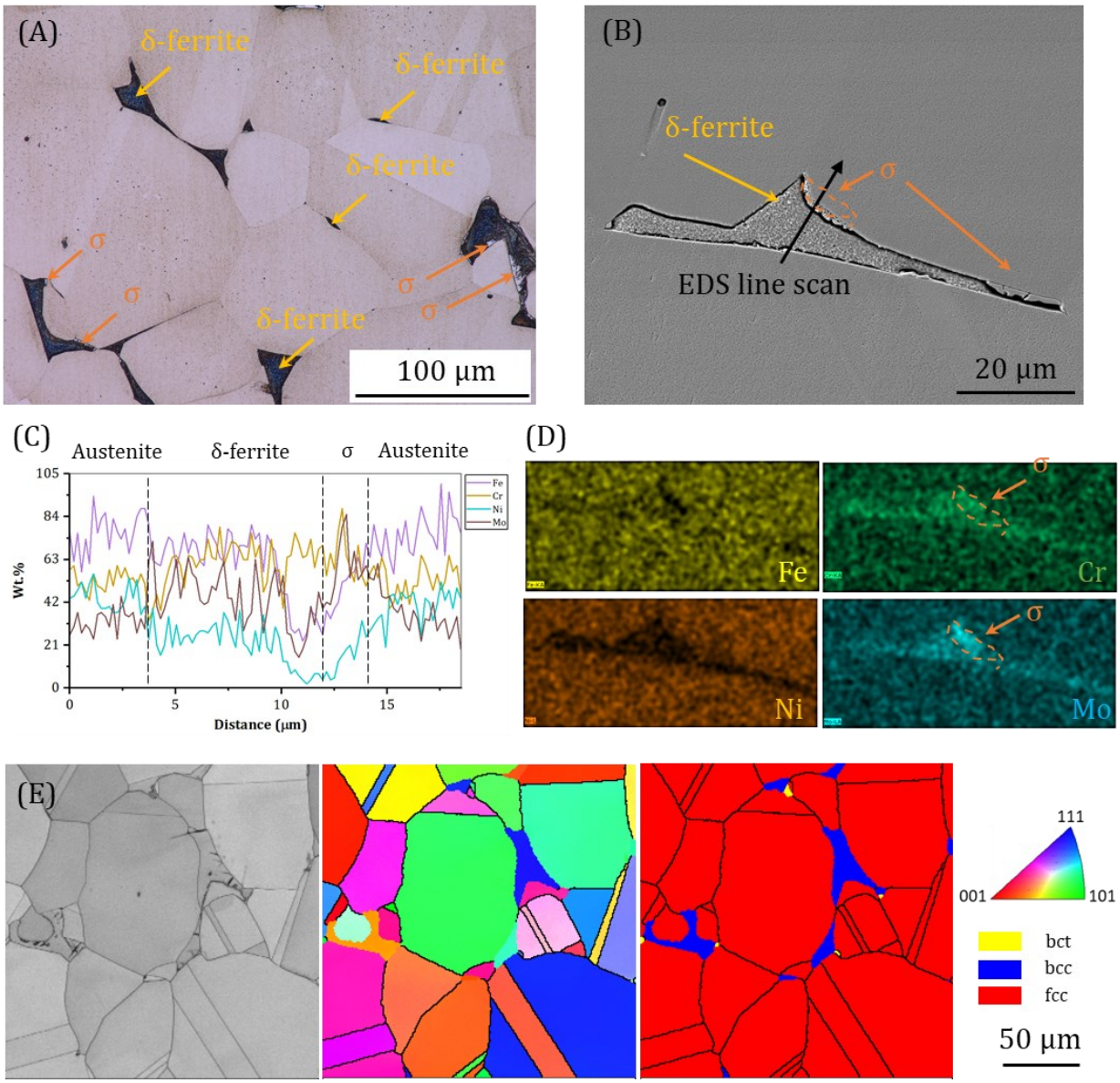

Figure 10. (A) Optical micrograph of the etched binder jetted 316L SS sintered at 1430 °C. Austenitic grain boundaries, δ-ferrite, and σ phase at the grain boundaries were visible. Etchant solution: Beraha color etchant composed of 100 ml distilled water, 50 ml hydrochloric acid, 6 g ammonium bifluoride, and 1 g potassium metabisulfite. (B) Scanning electron micrograph showing δ-ferrite and σ phase at a grain boundary, (C) EDS line scan as indicated in "B", (D) EDS map on the selected area in "B", and (E) EBSD micrographs including (left) band contrast, (middle) pole figure, and (right) phase map showing the grain structure and formation of three phases in the microstructure.

Table 4. Composition analysis from grain and grain boundaries of the SEM micrograph in Figure 9. The values are based on the average and deviation of three measurements.

	Fe	Cr	Ni	Mn	Mo	Si
Grain	Bal.	15.3±0.4	12.2±1.0	2.2±0.6	2.3±0.4	0.8±2
Grain boundary	Bal.	22.3±0.6	5.9±0.2	2.7±0.5	4.5±0.3	1.1±0.1

3.4. Phase analysis by X-ray diffraction

Figure 11 showed phase analysis of 316L SS powder and sintered specimens at different temperatures using X-ray diffraction. Virgin powder showed austenite as the dominant phase and small fraction of δ-ferrite phase. The presence of δ-ferrite phase in powder could be related to fast cooling rate occurred in the production of gas atomized powder. Also, fine particles (<10 μm) could potentially have higher fraction of δ-ferrite because of faster solidification rate compared to coarse powders (10<x<22 μm). When parts were sintered (<1370 °C), the XRD patterns did not show any peaks associated with δ-ferrite phase. This is because of the negligible content of δ-ferrite which is less than 5% and it has no effect on diffraction pattern of the austenite. In this situation, advanced microscopy tools such as transmission electron microscopy or EBSD micrographs can be applicable to detect small fraction of δ-ferrite at the grain boundaries (the later one was used in the current study and results were shown in Figure 8 and Figure 10). Lecis et al. [1] demonstrated that the presence of δ-ferrite was not uncommon in 316L SS in which skeletal δ-ferrite with ~10 vol.% was detected in the microstructure of sintered part. They also reported when the higher binder saturation (55% vs. 70%) was used in the binder jetting process, the fraction of δ-ferrite was lower. This could be attributed to higher concentration of C (when the binder saturation is set at higher numbers) as an austenite-promoting element, thus, fraction of δ-ferrite could decrease at the grain boundaries [5]. This was in agreement with results in this study in which the binder saturation of 80% was used to fabricate parts and the EBSD phase analysis showed formation of ~2% δ-ferrite in the microstructure of final part sintered at 1400 °C.

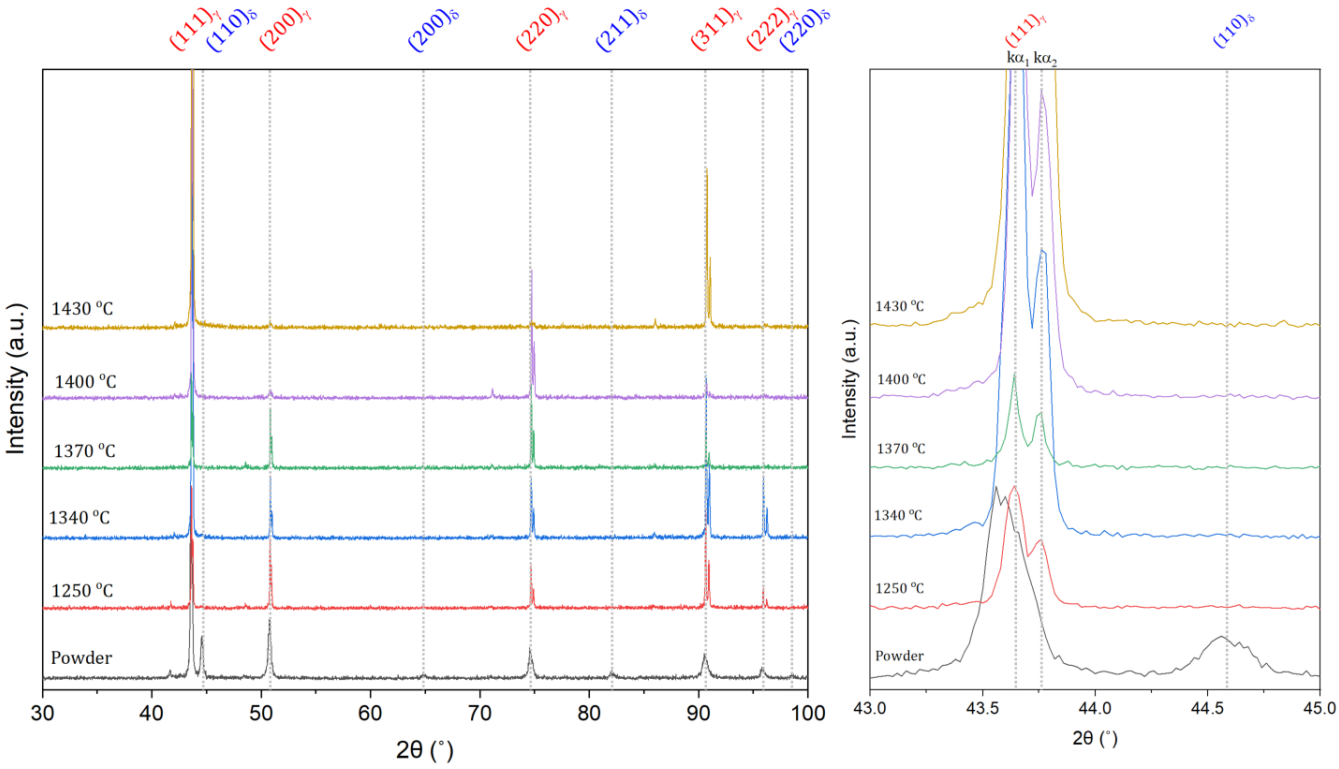

Figure 11. X-ray diffraction patters of the feed stock 316L SS powder, and binder jetted parts followed by sintering at different temperatures and holding time of 2 h.

3.5. Mechanical testing

Tensile tests were carried out on specimens sintered at various temperatures to study the porosity-strength-ductility relationships, and the representative stress-strain curves were shown in Figure 12. The average values of the 0.2% yield strength (*YS*), ultimate tensile strength (*UTS*), and elongation at failure (%) were listed in Table 5, and results were compared with conventionally- and additively-manufactured 316L SS alloy. It was evident that when the sintering temperature increased from 1250 °C to 1430 °C, the strength and ductility increased. The maximum *YS*, *UTS*, and elongation values of 201 MPa, 577 MPa, and 94% were achieved at the sintering temperature of 1430 °C, in which a relative density of 99.2% was achieved. Also, a reasonably high mechanical strength and ductility in the sample sintered at 1400 °C was observed. In fact, the homogeneous, equiaxed, and fine grain structure and high relative density of 99.4% obtained at 1400 °C allowed the sample to attain a good combination of mechanical strength and superior ductility (which exceeded the UNS S31603 standard requirements [27]). The parts sintered at temperatures above 1370 °C showed a comparable behavior in the elastic and elasto-plastic regions of the stress-strain curves. This would be an advantage at an industrial level in which a minimum *YS* and *UTS* as well as ductility are required.

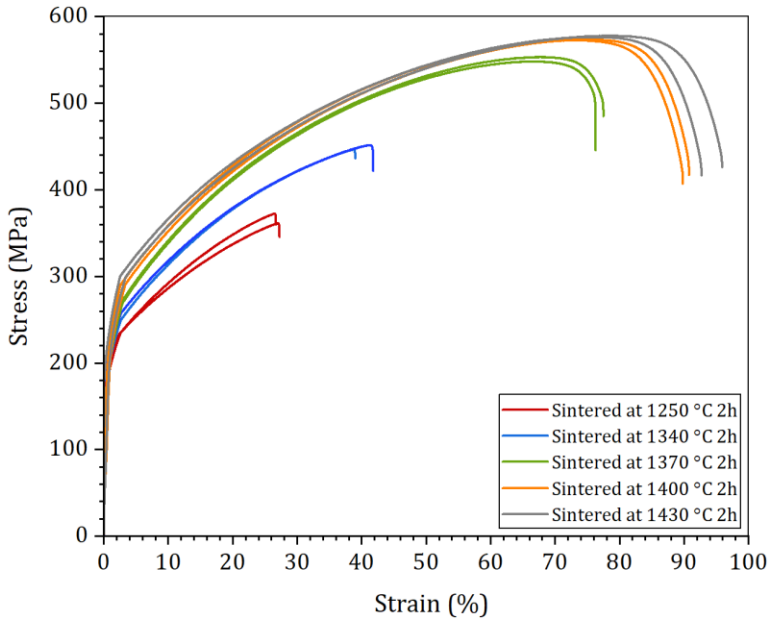

Figure 12. Stress-strain diagram of the binder jetted 316L SS sintered at different temperatures.

Table 5. Summary of the mechanical properties of the 316L SS alloy manufactured via different techniques.

Manufacturing process		Mechanical properties					Ref.
		YS	UTS	Elongation	Hardness	Relative density	
		[MPa]	[MPa]	[%]	[$HV_{0.5}$]	[%]	
Binder Jetting	Sintering at 1430 °C for 2 h	201.2±2.5	577.3±0.7	94.3±1.6	135±6	99.2±0.02	Present study
	Sintering at 1400 °C for 2 h	201.9±5.2	573.4±0.5	90.3±0.5	132±7	99.4±0.1	
	Sintering at 1370 °C for 2 h	198.6±6.5	550.8±2.5	76.9±0.6	127±7	97.7±0.4	
	Sintering at 1340 °C for 2 h	186.1±1.4	449.1±2.5	40.4±1.4	107±4	91.8±1.2	
	Sintering at 1250 °C for 2 h	130.4±27.8	366.9±5.5	27.0±0.3	84±4	83.7±0.6	
	Sintering at 1380 °C for 2 h	191±8	544±25	73.0±2.8	138±4	98.1±0.1	[27]
	Sintering at 1360 °C for 3 h	176±1	535±9	49±7	148±11	97.7	[1]
MIM	Sintered at 1300 °C for 3 h	~200	410±18	22±1	-	-	[28]
Fused filled filament		155-165	500-520	32-37	-	98-99.5	[29]
Extrusion 3D printing		166	524	96	-	98.7	[30]
Laser powder bed fusion		554±5	685±5	36±2	-	100	[31]
		420-520	550-640	30-70	210-240	98-99.9	[32]
Direct laser deposition		405-415	620-660	32-40	-	99.9	[33]
Wire arc additive manufacturing		235±6	533±23	48	-	100	[34]
Wrought		170	425	40	210	100	[35]
Cast		310	620	50.0	185	100	[35]

Morphology of the porosities, size of the grain, and fraction of phases are three influential factors that could account for the increasing levels of mechanical properties as the sintering temperature elevated [22]. N. Kurgan [36] showed that the mechanical strength of the sintered 316L SS (produced by powder metallurgy) had an inverse relation with porosity since pore size and its shape could be directly altered by sintering conditions. In other words, pores can result in localized stress rise, and subsequently an onset of plastic deformation at a lower stress level. Also, the phase fraction of the γ-austenitic grains and skeletal δ-ferrite at the grain boundaries could impact mechanical properties when the relative density is high. Muterlle et al. [37] observed that the fraction of δ-ferrite in the 316L SS manufactured by metal injection molding (MIM) followed by sintering at 1380 °C (with a relative density of 99.8%) was higher than that of MIM part sintered at 1360 °C (with a relative density of 98.5%) (i.e., 4.5% vs <1%), and presence of a higher amount of such a phase promoted the *YS*, *UTS,* and especially the ductility. In the same manner, in this study in which the δ-ferrite phase existed in the samples sintered at temperatures beyond 1370 °C, the *YS* and *UTS* increased and a significant upgrade in the elongation value was seen. Regarding the difference between the elongation of the 316L SS manufactured through the sintered-based and fusion-based AM processes, ~70% higher ductility was attained via the binder jetting. The reason could be associated with the higher fraction of annealing twins in the microstructure of the sintered parts [38].

Microhardness results indicated that the average hardness values increased from 84±4 $HV_{0.5}$ to 135±6 $HV_{0.5}$ as the sintering temperature increased from 1250 to 1430 °C (see Table 5). Although the hardness values can be explained by the Hall-Petch relation [1,27], both grain size and porosity level impact the hardness results. Firstly, the binder jetted 316L SS sintered at 1250 °C had a mean grain size of 9.6 μm and porosity of ~16% with a measured microhardness of 84±4 $HV_{0.5}$. As the sintering temperature increased to 1340 °C, the porosity fraction decreased to ~8% while the mean grain size increased to 19.6 μm leading to a measured microhardness of 107±4 $HV_{0.5}$. At the sintering temperature of 1370 °C, the porosity reduced to ~2.3%, mean size of the grain increased to 32.8 μm, and a microhardness value of 127±7 $HV_{0.5}$ was obtained. This observation clearly manifested that the Hall-Petch relation does not consider the effect of porosity fraction and it should be only used when the porosity of the material is a constant or pre-determined parameter in a study. As the sintering temperature increased to 1400 °C and 1430 °C, the porosity fraction decreased to 0.6% and 0.9% with a mean grain size of 32.2 μm and 38.3 μm, respectively. The difference between the hardness values of the samples sintered at such temperatures is not significant since the number and size of the pores are at the minimum values, thereby collecting the majority of the indentations within the grains.

Fractography was carried out on the specimens after the tensile test, and representative fracture surface micrographs were illustrated in Figure 13. At low sintering temperatures of 1250 °C and 1340 °C, the relative density was ~84% and 92%, respectively, and the horizontal print lines were visible on the fracture surface. Also, the side view of such fracture surfaces did not present any sign of necking suggesting a low-ductility fracture surface (potentially mixed ductile-brittle fracture) due to high porosity fraction resulting in failure at lower strain levels. Generally, porosity has a detrimental influence on the *YS* and ductility which would be related to the reduced area supporting the load and the stress concentration factor at each pore. The close-up view around a pore revealed a small amount

of plastic deformation with a high number of shallow dimples. These voids could be the origin of the early failure of the specimens sintered at low temperatures.

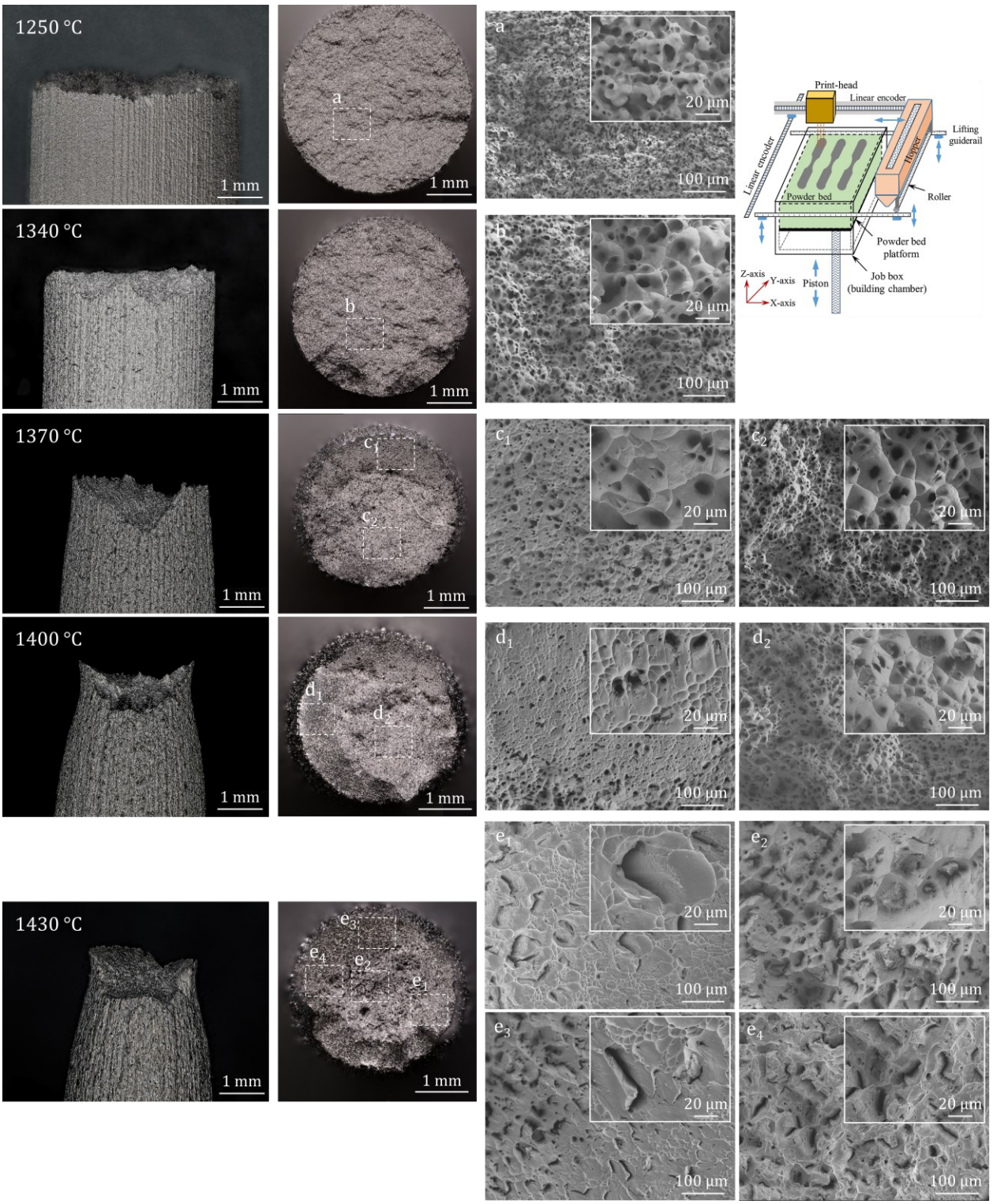

Figure 13. Optical images of the (left) side view, (middle) eagle top view of the fracture surface of the tensile specimens, and (two right columns) details on the fracture surfaces collected by FESEM. Print layout of parts are schematically illustrated.

As the sintering temperature was set at ≥1370 °C, necking was obvious from the side view of the fracture surfaces indicative of a shear fracture. Also, dimples were visible on all these fracture surfaces which are typical of a ductile fracture. In the part sintered at 1370 °C, the entire fracture surface was characterized by dimples [5,27], and the fracture morphology did not present any feature related to δ-ferrite phase. On the more ductile samples, sintered at 1400 °C and 1430 °C, the close-up view at different areas indicated the presence of a high number of dimples at the center of the fracture surface while a higher shear loading on the edges formed shallower dimples known as parabolic dimples [30]. Also, no second-phase particles were seen at the center of the dimples. At the highest sintering temperature of 1430 °C, a combination of deep dimples (ductile fracture) as well as secondary central cracks and parabolic dimples (due to a high shear fracture) was found at the fracture surfaces. High elongation of the samples sintered at 1400 °C and higher temperatures could also be associated with the superior work hardening behavior in the 316L SS dominated by twinning and cross-slip mechanisms, thereby leading to an enhanced dislocation density and higher ductility [5]. This will be discussed in section 3.6.

3.6. Sintering regimes and microstructure-defect-property relationships

The final microstructure and resultant mechanical properties of the binder jetted metals mainly rely on the final density, pore morphology, grain structure, and phase fraction. Using fine metal powder (i.e., mean size of 10.7 μm) in a binder jetting system requires an effective powder dispensing system to maximize the powder bed density/uniformity and minimize powder agglomeration [20]. Temperature, holding time, and atmosphere of the sintering play a crucial role in the densification and subsequent pore removal of the part. Also, the green part density directly affects the final density of the sintered body. Two sintering mechanisms of solid-state sintering and SLPS have been studied. To ensure that a binder jetted component with a complex geometry retains its shape after the sintering process, the fraction of the liquid phase should be limited to ~2-5%.

Generally, sintering is performed under inert gas (i.e., N_2 and Ar), reducing atmosphere (i.e., H_2), or vacuum conditions. Nitrogen can be absorbed by iron and form nitride, which negatively impacts the mechanical properties. Also, there is a possibility of Ar entrapment in pores, thereby hindering densification in the final stage of the sintering. A reducing atmosphere such as H_2 might be ideal for sintering of an active metal such as copper; however, there is a possibility of the existence of trapped H_2O in the intermediate stage of the sintering which again hinders the final stage of the sintering. Therefore, to enhance densification, vacuum sintering is preferred for the binder jetted metals. Not only does vacuum sintering minimize the formation of the gas-filled pores and oxidation, but it also assists in the reduction of carbon contamination [39]. In the final stage of sintering, the sintering rate remarkably decreases and pore healing occurs by lattice diffusion of vacancies through Nabarro-Herring mechanism [40,41]. Also, it should be noted that the applied sintering temperature could result in the liquid formation locally which accelerates the densification rate. This will be effective when there is no gas pore within the powder particles. During vacuum sintering, evaporation-condensation actively begins in the initial

stage of sintering and continues in the final densification stage in which material removal from the convex surface of the pore to the concave surface of the pore is eased. This could be an unwanted incident when evaporation of alloying element is accelerated by vacuum sintering [42,43]; however, vacuum sintering can eliminate excessive C (as well as N and O) added by polymer binder to the 3D printed 316L SS powder. Rios et al. [3,4] and Mostafaei et al. [19] showed that the excessive C, H, and N cause by polymer binder was eliminated during the sintering step. Overall, vacuum sintering can accelerate binder removal containing O and C during the burnout step at 450-600 °C, thereby effectively minimizing the contamination of the final part by such elements and limiting the formation of inclusions [1,27].

As discussed in section 3.1 and illustrated in Figure 2, the binder jetted fine powder showed inter-layer void defects formed because of powder-binder interactions. An earlier study [16] showed that when the green density of the fine powder is below 50%, the maximum relative density of the sintered body reaches about 98%; however, by the help of ultrasound recoater and double rollers, powder packing density was enhanced, and a relative density of ~54% was attained which led to densities of >99% at sintering temperatures ≥1400 °C. *"**The initial stage of sintering**"* takes place at low temperatures in which necks form at the contacting powder surfaces. Evaporation-condensation and surface diffusion are known as active non-densifying mechanisms, and minimal dimensional variation and pore removal is expected. When fine 316L SS powder is used, this stage starts at an extremely low sintering temperature of ~1000 °C [4]. Therefore, the applied sintering temperature of 1220 °C was already in "***the intermediate stage of sintering***." This stage proceeds with the neck growth and pore-filling actions leading to more discontinuous pore sections in 2D as displayed in Figure 4C. During this stage, elongated pores will be evolved into the fine equiaxed pores, and the density of the sintered part remains below 90-92%. This stage continues up to a sintering temperature of 1355 °C (see Figure 14A). Plastic flow, lattice diffusion, and grain boundary diffusion could be the active densifying mechanisms at this stage. "***The final stage of sintering***" begins at the temperature of 1370 °C and higher in which pore closure occurs, and microstructure enters the final stage of the densification (i.e., >95%). Grain growth is possible if the holding time is over 2 h. The virgin powder showed a solidus temperature of ~1433 °C, however, the presence of C in binder could locally reduce the solidus at temperatures of >1366 °C [1].

Based on the Schaeffler and Pseudo-binary diagrams for steels [44] (see Figure 14B), the microstructure of the 316L SS alloy consists of γ-austenite grains with a trace amount of δ-ferrite at the grain boundaries. The calculated equivalent Ni and Cr content of the binder jetted 316L SS was 21.3 wt.% and 12.9 wt.%, respectively. For the given composition of the used 316L SS alloy in this study, there is a possibility of σ phase (enriched in Fe-Cr-Mo) formation adjacent to the δ-ferrite at the grain boundary (see Figure 10). In samples sintered at temperatures of 1220-1355 °C, no grain boundary δ-ferrite was observed in the optical and scanning electron micrographs while the parts sintered at ≥1370 °C showed liquid phase formation at the grain boundaries, which were characterized as δ-ferrite. It was reported in [45,46] that the σ phase forms due to the decomposition of the δ-ferrite upon slow cooling

below ~900 °C; therefore, there is a possibility for the formation of σ phase in the parts sintered at 1370 °C and higher.

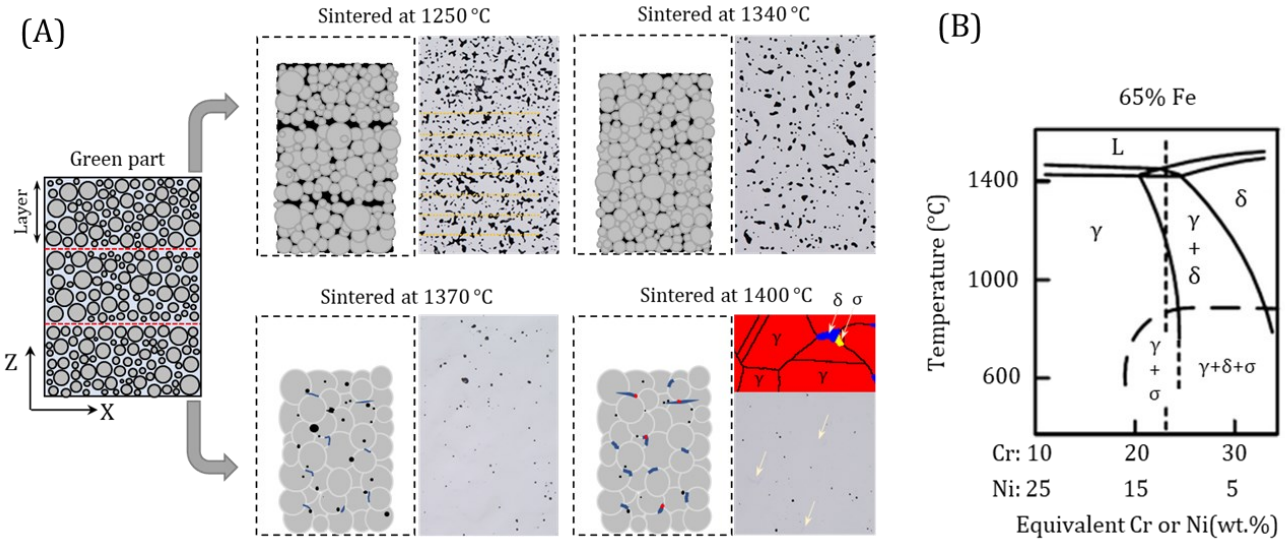

Figure 14. (A) Schematic illustration of the densification mechanisms against sintering temperature. Print layers were shown by dash lines in the as printed part and sintered at 1250 °C. Also, yellow arrows showed presence of δ-ferrite (due to SLPS) and σ phase (due to slow cooling rate) at the grain boundaries. (B) Fe-Cr-Ni pseudo-binary phase diagram at 63% Fe. Below the 900 °C, σ phase may form due to slow cooling rate.

As indicated in Table 5, the *UTS* of the binder jetted 316L SS alloy was ~5-10% lower than the cast and LPBF-processed alloy while the *YS* was ~30% lower than the cast alloy and 60% of the LPBF-processed one. These discrepancies were associated with the grain size (d) and porosity fraction in the sintered parts. Dependency of the *YS* to d can be explained by the Hall-Petch relationship:

$$\sigma_y = \sigma_0 + K_y(d)^{-0.5} \quad (5)$$

where σ_y is *YS*, σ_0 is the frictional stress hindering dislocations glide, K_y is the locking parameter (*a.k.a.* a measure of lattice resistance to the slip), and d is the grain size. The analyzed grain size of the sintered binder jetted 316L SS specimens in this study were compared with the grains size of the conventionally (e.g., cast [47], cold-rolled [48], hot isostatic pressed [49]) and additively-manufactured parts (e.g., LPBF [5,48]), and results were demonstrated in Figure 15A. The applied linear fit with R^2>0.95 was used to extrapolate $\sigma_0 = 161.53$ MPa and $K_y = 301.64$ MPa.(μm)$^{0.5}$. The relation suggests that the maximum *YS* in the LPBF parts was related to the fine solidification cell structure (i.e., 0.5<d<2 μm) while the conventionally or binder jetted parts showed a coarse grain structure (i.e., 10<d<50 μm). It is noteworthy that the Hall-Petch relationship is valid when part is fully dense. Typically, remnant pores are seen in the sintered binder jetted parts; hence, deviation of the *YS* from the calculated values seems reasonable (lowered by 10-25% depending on the porosity fraction). This can be explained by the fact that pores acts as stress concentrators which causes a locally increased stress, and plastic deformation at lower stress levels accordingly [36]. To estimate the *YS* of a porous ferrous structure, the following equation can be used [50–53]:

$$\sigma_y = \sigma_{y,0} \times \exp(-6.5\, f) \quad (6)$$

where $\sigma_{y,0}$ is the *YS* of a fully dense 316L SS alloy, and f is the pore volume fraction. In this equation, the $\sigma_{y,0}$ value is calculated from the fitted linear line on the *YS* versus grain size plot (see Figure 15A). Based on the analyzed grain size (Figure 9C) for the differently sintered binder jetted 316L SS alloy, the *YS* was estimated (using Eq. 5) to be 210-215 MPa for the high-density parts (1370-1430 °C). Using Eq. 6, the estimated *YS* was 202-207 MPa, in agreement with the measurement reported in Table 5.

316L SS is characterized as a ductile material and yields at low stresses; therefore, considerable strain (work) hardening behavior could be observed. Strain hardening phenomenon occurs in the plastic region beyond the *YS* point and is ended before the necking starts. As the sample passes the *YS* point, the initial stage of low hardening could be detected by the planar glide of the dislocations [54]. Proceeding in the plastic strain, the density of the dislocations will be increased, which causes resistivity in their mobility leading to cross-slip, thereby creating dislocation cells. Such an alteration results in a second stage of hardening in the material with a noticeable higher hardening rate [55,56]. It should be noted that in 316L SS, twinning also plays a role during plastic deformation.

To study the strain hardening behavior, the plastic flow of the true stress-strain response was plotted (see Figure 15B,C) after converting the engineering stress and strain data into true stress and strain by the following formulas:

$$\sigma_{true} = \sigma_{engineering} \times (1 + \varepsilon_{engineering}) \quad (7)$$

$$\varepsilon_{true} = ln(1 + \varepsilon_{engineering}) \quad (8)$$

The two-stage strain hardening is predominantly seen in the 316L SS [5,55] which was formulated by the mathematical model of Ludwigson as below [55]:

$$\sigma = K_1.\varepsilon_P^{n_1} + e^{K_2 + n_2.\varepsilon_P} \quad (9)$$

where σ and ε_P are described as true stress and true plastic strain, K_1 and K_2 are strength factors (strain hardening coefficients), and n_1 and n_2 are the strain hardening exponents. This equation is an appropriate fit for various FCC metals with a low stacking fault energy, e.g., stainless steels [54]. Here, the first term describes the cross-slip deformation mode and deformation twinning at larger strains, and the second term corresponds to the planar dislocation glide at lower strains. In the FCC metals, the motion of the mobile dislocation can be hindered by obstacles; thus, an increase in dislocation density would enhance the work hardening rate because of the higher possibility of resistance to dislocation motion.

To extract the exponents and coefficients, Ludwigson's nonlinear equation (Eq. 9) was fitted to the curves shown in Figure 15C, and the results were summarized in Table 6. Three factors of grain size, stacking fault energy, and the existence of the δ-ferrite phase were emphasized to affect the strain hardening behavior [5,54]. The calculated values of K_1 and n_1 (slope of the second stage of strain hardening) showed a declining trend when the sintering temperature decreased from 1430 °C to 1250 °C. It is noteworthy that when the density reaches >99% (at sintering temperatures of 1400 °C and higher), the values of K_1 (1515 MPa) and n_1 (0.71) showed negligible changes. A cold-rolled strip of 316L SS with a grain size of ~3 μm had an n_1 of 0.37 while a binder jetted part with a grain size of 32 μm had an n_1 of 0.71.

Singh et al. [54] noticed that when the grain size is <6 μm, the variation of n_1 between 0 and 1 was significant. In contrast, the grain size of >6 μm showed minimal changes as observed in the binder jetted 316L SS. The binder jetted 316L SS specimens had an initial low hardening rate related to the planar dislocations glide followed by a higher strain hardening rate at larger strains related to cross-slip and twinning deformation. In other words, dislocation density increased due to the plastic deformation at the secondary stage, leading to a higher resistance to dislocation motion, thereby activating the cross-slip and twinning deformation.

The SFE can be used as an indicator of deformation mechanism in 316L SS alloy. At SFE of ~15–45 mJ/m^2, twining deformation mechanism is dominant, while, at high SFE ≥ 45 mJ/m^2, dislocation glide is the major deformation mechanism. An approximate estimate of the SFE for parts sintered at ≥ 1400 °C was attained using the JMatPro software based on the chemical compositions analysis given in Table 3 and Table 4. The SFE values were found to be ~32±3 mJ/m^2 for the matrix (γ grains) of the binder jetted parts (ambient temperature), thus, the predominant deformation mechanism was twining. This does not contract the earlier discussion using Eq. 9. Kumar et al. [5] binder jet printed the same powder followed by sintering at 1380 °C for 2 h. The estimated SFE was ~ 48 mJ/m^2 because authors assumed that the composition of C, N, O, and S in the final densified part was similar to the virgin powder, however, chemical analysis in the current study (see Table 3) revealed that the composition of these interstitial elements (C, N, O) dropped in the sintered part which noticeably reduced the estimated SFE.

The presence of the grain boundary δ-ferrite was thought to be another influential factor in high strain hardening behavior of binder jetted 316L SS specimens. Since closed-pack planes available in the FCC crystal structure are not present in the BCC crystal structure, the δ-ferrite phase is notably harder compared to the γ-austenite phase, which causes plastic deformation to occur at different sequences in such phases. Based on the Kurdjomov-Sachs orientation relationship, the retained grain boundary δ-ferrite confronted $[110](1\bar{1}1)_\gamma//[111](1\bar{1}0)_\delta$ to ease the interphase slip transfer. To be more specific, the γ-austenite phase deforms at lower strains while the slip transfers to the δ-ferrite phase at higher strains, thereby forming dislocation mobility, greater work hardening, and higher ductility [57,58]. Therefore, the presence of the δ-ferrite phase at the sintering temperatures of ≥1370 ℃ could account for such higher n_1 values in this study compared to the given values in Table 6.

In 316L SS, plastic deformation was related to dislocation gliding followed by a cross-slip. The transitioning step between these two mechanisms can be extracted from the work hardening rate ($d\sigma/d\varepsilon$) against the true plastic strain plot (see Figure 15D and Table 6). The true transition strain, ε_T, at which flow transition from the planar glide to duplex slip takes place, were attained based on the point-tangent intersection. It was seen that the ε_T was ~0.79±0.01% in part sintered at 1250 °C and increased to 1.53±0.03% at the sintering temperature of 1430 ℃. The corresponding engineering stress of the transition point, σ_T, was 204.40±2.58 MPa (sintered at 1250 °C) and increased to 306.49±4.66 MPa (sintered at 1430 °C). Such values of ε_T and σ_T were reported to be ~2.37±0.3% and 253±13 MPa for the binder jetted parts and 1.57% and 359 MPa for the conventionally manufactured part [5]. The

results showed that by the increase of the sintering temperature, the transition point of the glide deformation and duplex slip occurred at higher values of stress and strain.

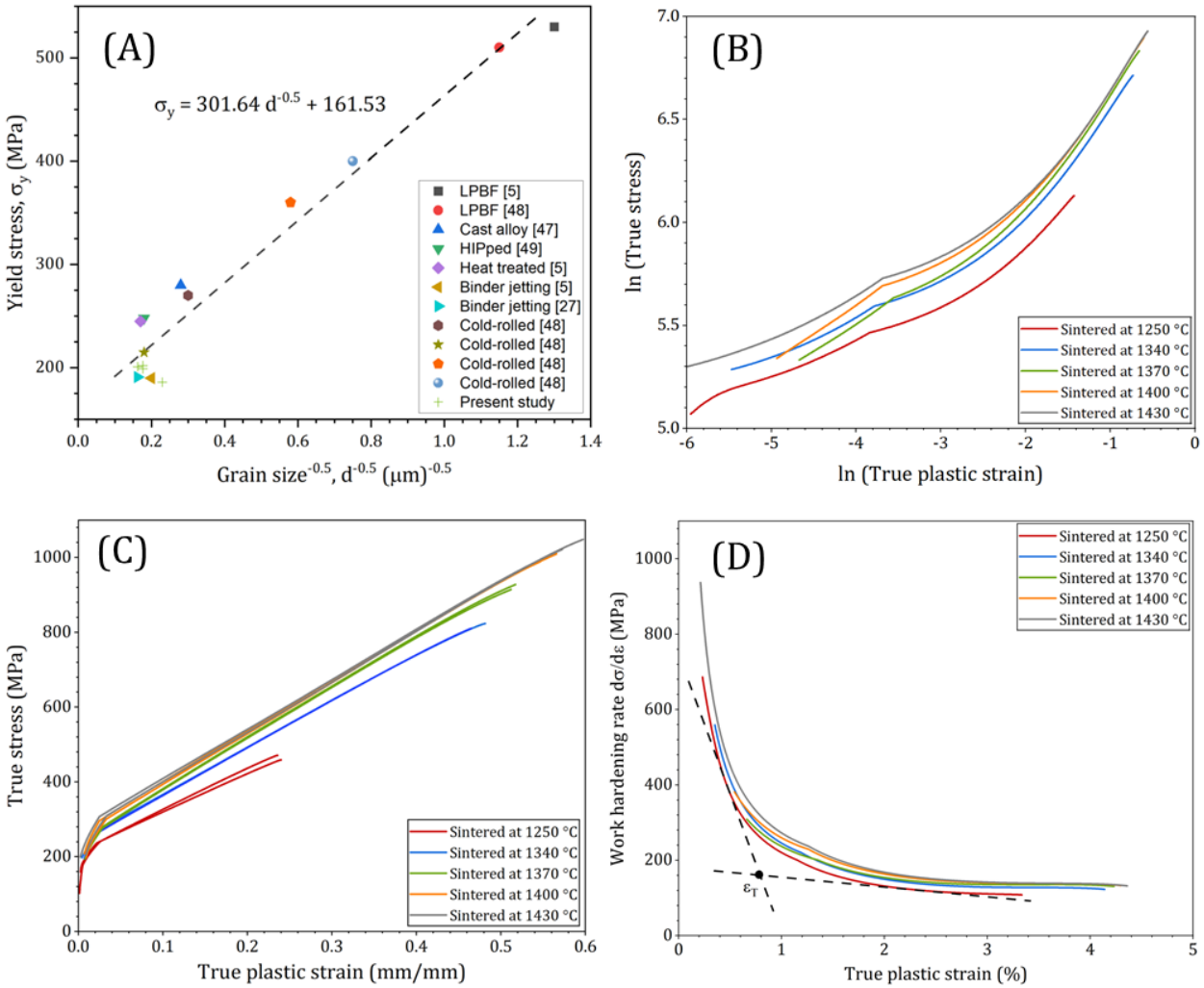

Figure 15. (A) Hall-Petch plot showing *YS* versus grain size for the 316L SS alloy manufactured via different techniques, (B) natural logarithm plot of the plastic strain versus true stress presenting the strain hardening behavior, (C) experimental true plastic strain versus true stress data fitted using the Ludwigson constitutive model, and (D) work hardening rate ($d\sigma/d\varepsilon$) against the true plastic strain plot.

Table 6. Constants of Ludwigson's constitutive relationship for the two-stage strain hardening of the binder jetted 316L SS samples sintered at different temperatures. For comparison, data from literature was also added to this table in which the grain size of the specimens was 26 μm.

Sample	**Constants of Ludwigson's constitutive relationship**				**Ref.**
	K_1 (MPa)	**n_1**	**K_2 (MPa)**	**n_2**	
1430 °C for 2h	1511±2	0.701±0.002	5.341±0.002	-6.8±0.1	Present study
1400 °C for 2h	1510±2	0.701±0.002	5.291±0.002	-6.9±0.1	
1370 °C for 2h	1461±1	0.683±0.001	5.179±0.001	-8.1±0.1	
1340 °C for 2h	1330±1	0.649±0.001	5.190±0.001	-9.7±0.1	
1250 °C for 2h	930±4	0.499±0.003	4.865±0.006	-15.7±0.3	
1380 °C for 2h	1317±31	0.531±0.004	4.958±0.064	-19.5±1.9	[5]
Cold-rolled	1291.7	0.37	5.2	-54	[54]

The effect of uniaxial tensile test on the work hardening, microstructure, and porosity/void evolution was studied and the results were shown in Figure 16. The hardness increased by moving toward the fracture surface, i.e., increasing the amount of plastic deformation (see Figure 16A). The higher rate of plastic deformation results in higher rate of work hardening by means of dislocation movement or dislocation generation. The predominant deformation mechanism in FCC alloys with low stacking fault energy (SFE) is considered to be twinning [59]. Here, by using EBSD data, the effect of plastic deformation rate on the microstructure of the parts was shown in Figure 16B,C. The lowest amount of plastic deformation (i.e., far from the fracture surface) resulted in local increase in misorientation around the porosities and inside the grains, particularly, around the annealing twins. It was apparent that the grain structure was equiaxed far from the fracture surface (on the left side of Figure 16A, ~10 mm far from the fracture surface, as demonstrated by EBSD results in Figure 16B), while, elongated grains dominated microstructure of the area closer to the fracture surface which were indicative of severe plastic deformation of grains and enhanced misorientation in grains (as demonstrated in Figure 16C). By increase in plastic deformation, the annealing twins started to disappear and converted to high angle grain boundaries by relative rotations exceeding Brandon's criterion [60], and new deformation twins started to be generated. By further increasing the plastic deformation, the newly generated twins started to decay and be converted into new high angle grain boundaries. In addition, the twinning is dependent on the grain size regardless of the twinning type [61]. The decrease in the grain size is obvious by moving closer to the fracture surface; thus, the lower number of twins in this region can also be justified by lower grain sizes in this region.

Pore distribution analysis using μ-CT on the failed specimen were shown in Figure 16D. Firstly, majority of the nucleated/grown voids concentrated in the central region and close to the fracture surface of the specimen (see Figure 16d_2). Elongated voids were ellipsoidal and most of which were oriented in the tensile direction, and the density of pores/voids increased towards the fractured surface (see Figure 16d_4). Optical microscopy observations revealed that high concentration of strain causes more voids to nucleate in the δ-ferrite regions as shown in Figure 16a_1,a_2. The higher strength of δ-ferrite compared to γ-austenite and its BCC crystal structure (with lower active slip systems compared to FCC) were responsible for void nucleation and growth in areas composed of δ-ferrite at the grain boundaries. Typically, the growth rate of voids in the tensile direction under triaxial stress was rapid, as observed for the necked tensile specimen in Figure 16d_4,d_5. Meanwhile, voids were inclined to grow and finally coalesce in the direction perpendicular to tension, resulting in the carack formation and failure. In addition, it was seen in Figure 16d_1,d_4 that the fracture surface that the deformation bands were generated 45° from the tensile axis with cracking at the center.

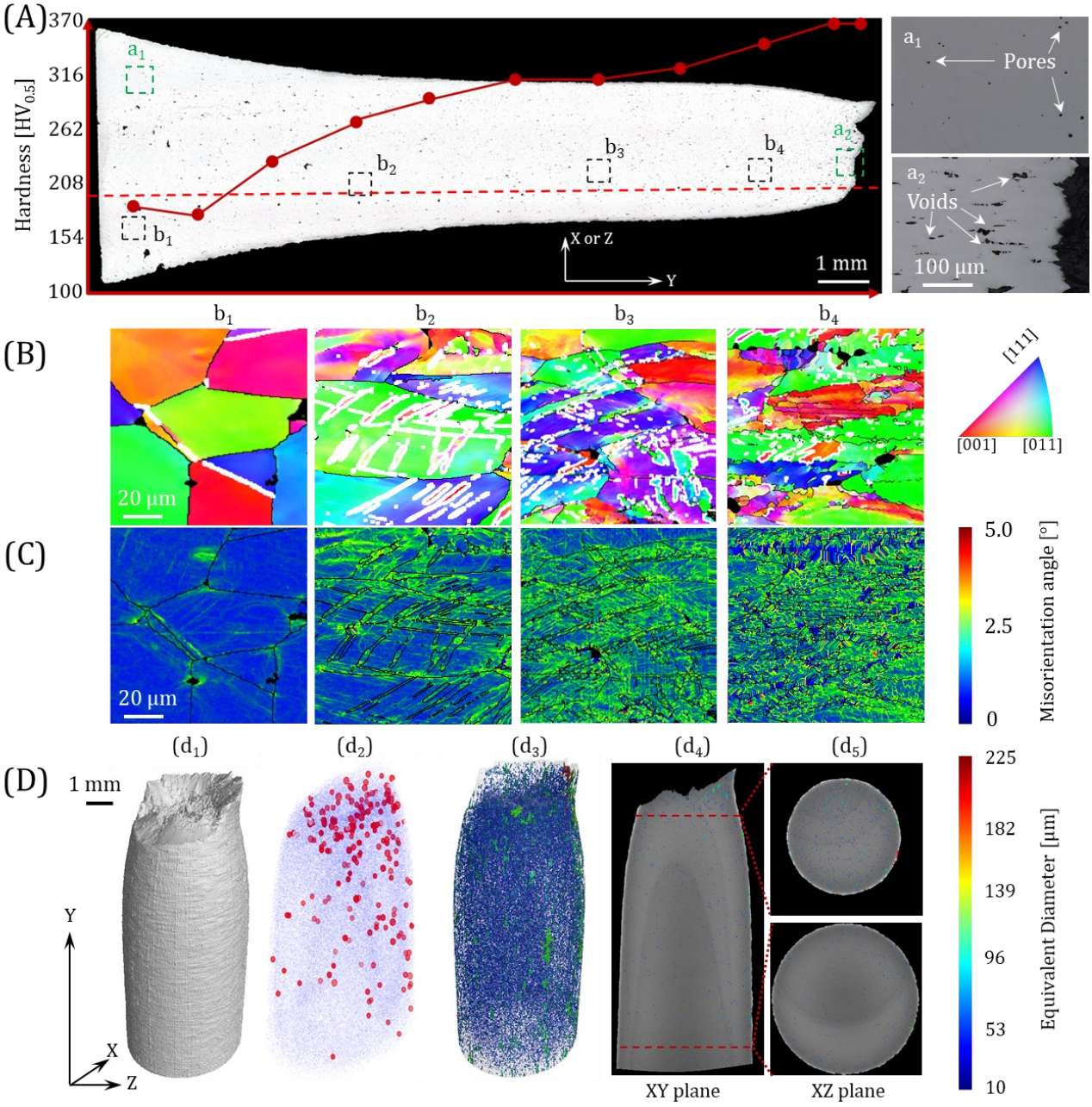

Figure 16. (A) Vickers microhardness results on the cross-section of the specimen after tensile test. The effect of plastic deformation on the work hardening was obvious based on the increased hardness by moving toward the fracture surface. The hardness results were collected on the red dash line. Also, a_1 and a_2 demonstrated optical micrographs to visualize remnant pores after sintering vs. generated voids in δ-ferrite due to uniaxial tension. Microstructure analysis using EBSD: (B) IPF-Z maps and (C) kernel average misorientation (KAM) maps on the cross-section of the specimen after tensile test. Note that the EBSD data in (B,C) are correspondent to the black dashed squares in (A) from left to right – labeled as b_1 to b_4, and the white lines in EBSD IPF-Z maps represent twinning lines. (D) μ-CT results of the tensile sample after failure showing (d_1) the fracture surface, (d_2) Projected pore area on XY plane and red circles show pores with projected area larger than 5000 µm^2, (d_3) spatial distribution of pores in the failed part showing pore fraction of 1.09% after tensile test, (d_4,d_5) 2D shadow projection on the XY and XZ planes showing distribution and size of pores in the failed tensile specimen. The sample was sintered at 1400 °C for 2 h.

4. Conclusions

A comprehensive study was performed on the microstructure-defect-property relationships of the vacuum-sintered binder jetted fine 316L austenitic stainless steel powder. In summary, the following conclusions can be drawn:

1. Sintering was conducted on as-printed parts with relative densities of ~54%, and the highest density of 99.4% was attained after SLPS at 1400 °C for 2 h. Regardless of the applied sintering temperature, anisotropy shrinkage was seen in all samples, and a maximum linear shrinkage of 18.4%, 17.7%, and 21.5% in *X*-, *Y*-, and *Z*-directions was obtained.
2. Surface topology assessment using SEM showed open pores on the surface in agreement with the apparent density measurements, and the number of pores (based on optical micrograph analysis) significantly decreased as the sintering temperature increased to 1400 °C. Also, the optical profilometry showed an average roughness (R_a) of 1.6 μm in the as-printed part which decreased to 1.0 μm in the specimen sintered at 1400 °C for 2 h.
3. Microstructure observations using EBSD demonstrated grain evolutions as a function of sintering temperature. A fine grain size of ~10 μm was observed at relatively low sintering temperatures (<1300 °C), and average grain size of ~32 μm was seen at sintering ≥1370 °C). In all sintered parts, a uniform and homogenous grain size and pore distribution was seen at the *XZ* cross-sections confirming a uniform microstructure evolution during sintering. In addition, δ-ferrite appeared at the grain boundaries in samples sintered ≥1370 °C, in which the fraction was at most ~3%. Due to the slow cooling nature of the binder jetted parts in the tube furnace, a trace amount of σ phase was detected in the EBSD micrographs of sintered parts at 1400 °C and higher.
4. Mechanical testing showed tensile strength, yield strength, elongation, and hardness of 202 MPa, 573 MPa, 90%, and 132 $HV_{0.5}$, respectively, in the part sintered at 1400 °C for 2 h. Fractography revealed the formation of deep dimples at the center as well as secondary central cracks and parabolic dimples (due to a high shear fracture) at the edges. Superior elongation value was related to the combined two-stage work hardening dominated by twinning deformation mechanism, the presence of δ−ferrite phase up to 2%.

Acknowledgements

AM would like to acknowledge the startup funding from the Department of Mechanical, Materials and Aerospace Engineering and Armour College of Engineering at Illinois Institute of Technology at Chicago, Illinois. Authors acknowledge partial support from the National Science Foundation under grant number DMR-2050916. The authors would like to acknowledge Dr. An-Chou Yeh's group in National Tsing Hua University for their assistance in phase prediction.

References

[1] N. Lecis, M. Mariani, R. Beltrami, L. Emanuelli, R. Casati, M. Vedani, A. Molinari, Effects of process parameters, debinding and sintering on the microstructure of 316L stainless steel produced by binder jetting, Mater. Sci. Eng. A. 828 (2021) 142108.

[2] R. Batmaz, A. Zardoshtian, T.D. Sabiston, R. Tangestani, A. Chakraborty, N. Krutz, S. Pendurti, A. Natarajan, E. Martin, An Investigation into Sinterability Improvements of 316L Binder Jet Printed Parts, Metall. Mater. Trans. A Phys. Metall. Mater. Sci. 53 (2022) 915–926.

[3] A.C. Rios, E. Hryha, E. Olesvsky, P. Harlin, Sintering anisotropy of binder jetted 316L stainless steel: part I – sintering anisotropy, Powder Metall. (2021).

[4] A.C. Rios, E. Hryha, E. Olesvsky, P. Harlin, Sintering anisotropy of binder jetted 316L stainless steel: part II – microstructure evolution during sintering, Powder Metall. (2022).

[5] P. Kumar, R. Jayaraj, J. Suryawanshi, U.R. Satwik, J. McKinnell, U. Ramamurty, Fatigue strength of additively manufactured 316L austenitic stainless steel, Acta Mater. 199 (2020) 225–239.

[6] Z. Chen, W. Chen, L. Chen, D. Zhu, Q. Chen, Z. Fu, Influence of initial relative densities on the sintering behavior and mechanical behavior of 316 L stainless steel fabricated by binder jet 3D printing, Mater. Today Commun. 31 (2022) 103369.

[7] G. Lewis, Properties of open-cell porous metals and alloys for orthopaedic applications., J. Mater. Sci. Mater. Med. 24 (2013) 2293–2325.

[8] S. Anderson, G. Baca, M. O'Connor, NEET-AMM Final Technical Report on Laser Direct Manufacturing (LDM) for Nuclear Power Components, 2676 (2015) Medium: ED; Size: 45 p.

[9] X. Lou, M. Song, P.W. Emigh, M.A. Othon, P.L. Andresen, On the stress corrosion crack growth behaviour in high temperature water of 316L stainless steel made by laser powder bed fusion additive manufacturing, Corros. Sci. 128 (2017) 140–153.

[10] A. Hemmasian Ettefagh, S. Guo, J. Raush, Corrosion performance of additively manufactured stainless steel parts: A review, Addit. Manuf. (2020) 101689.

[11] A. Mostafaei, P. Rodriguez De Vecchis, I. Nettleship, M. Chmielus, Effect of powder size distribution on densification and microstructural evolution of binder-jet 3D-printed alloy 625, Mater. Des. 162 (2019) 375–383.

[12] F. Bachmann, R. Hielscher, H. Schaeben, Texture Analysis with MTEX – Free and Open Source Software Toolbox, Solid State Phenom. 160 (2010) 63–68.

[13] E. Wheat, M. Vlasea, J. Hinebaugh, C. Metcalfe, Sinter structure analysis of titanium structures fabricated via binder jetting additive manufacturing, Mater. Des. 156 (2018) 167–183.

[14] A. Mostafaei, J. Toman, E.L. Stevens, E.T. Hughes, Y.L. Krimer, M. Chmielus, Microstructural evolution and mechanical properties of differently heat-treated binder jet printed samples from gas- and water-atomized alloy 625 powders, Acta Mater. 124 (2017) 280–289.

[15] Y. Zhu, Z. Wu, W.D. Hartley, J.M. Sietins, C.B. Williams, H.Z. Yu, Unraveling Pore Evolution in Post-Processing of Binder Jetting Materials: X-Ray Computed Tomography, Computer Vision, and Machine Learning, Addit. Manuf. (2020) 101183.

[16] C. Zheng, A. Mostafaei, P.R. de Vecchis, I. Nettleship, M. Chmielus, Microstructure

evolution for isothermal sintering of binder jet 3D printed alloy 625 above and below the solidus temperature, Addit. Manuf. 47 (2021) 102276.
[17] A. Mostafaei, P.R. De Vecchis, M.J. Buckenmeyer, S.R. Wasule, B.N. Brown, M. Chmielus, Microstructural evolution and resulting properties of differently sintered and heat-treated binder jet 3D printed Stellite 6, Mater. Sci. Eng. C. 102 (2019) 276–288.
[18] M. Salehi, S. Maleksaeedi, S.M.L. Nai, G.K. Meenashisundaram, M.H. Goh, M. Gupta, A paradigm shift towards compositionally zero-sum binderless 3D printing of magnesium alloys via capillary-mediated bridging, Acta Mater. 165 (2019) 294–306.
[19] N.D. Parab, J.E. Barnes, C. Zhao, R.W. Cunningham, A.D. Rollett, T. Sun, Real time observation of binder jetting printing process using high-speed X-ray imaging, Sci. Rep. (2019) 28–30.
[20] K. Myers, A. Paterson, T. Iizuka, A. Klein, The Effect of Print Speed on Surface Roughness and Density Uniformity of Parts Produced Using Binder Jet 3D Printing, Solid Free. Fabr. 2019 Proc. 30th Annu. Int. (2019) 122–133.
[21] A. Mostafaei, S.H.V.R. Neelapu, C. Kisailus, L.M. Nath, T.D.B. Jacobs, M. Chmielus, Characterizing surface finish and fatigue behavior in binder-jet 3D-printed nickel-based superalloy 625 Characterizing surface finish and fatigue behavior in binder-jet 3D-printed nickel-based superalloy 625, Addit. Manuf. 24 (2018) 200–209.
[22] A. Zwiren, Comparison of Binder Jetting Additive Manufacturing to Press and Sinter 316L Stainless Steel, (2018) Corpus ID: 150368018.
[23] B.P. Kashyap, K. Tangri, Grain growth behaviour of type 316L stainless steel, Mater. Sci. Eng. A. 149 (1992) 13–16.
[24] Y. Bai, C.B. Williams, Binder jetting additive manufacturing with a particle-free metal ink as a binder precursor, Mater. Des. 147 (2018) 146–156.
[25] A. Mostafaei, A.M. Elliott, J.E. Barnes, C.L. Cramer, P. Nandwana, M. Chmielus, Binder jet 3D printing - process parameters, materials, properties, modeling, and challenges, Prog. Mater. Sci. 119 (2021) 100707.
[26] D. Huber, L. Vogel, A. Fischer, The Effects of Sintering Temperature and Hold Time on Densification, Mechanical Properties and Microstructural Characteristics of Binder Jet 3D Printed 17-4 PH Stainless Steel, Addit. Manuf. (2021) 102114.
[27] S. Mirzababaei, B.K. Paul, S. Pasebani, Microstructure-property relationship in binder jet produced and vacuum sintered 316 L, Addit. Manuf. 53 (2022) 102720.
[28] M.F.F.A. Hamidi, W.S.W. Harun, N.Z. Khalil, M. Samykano, Microstructural comparison and mechanical properties of stainless steel 316L fabricated by selective laser melting and metal injection moulding processes, Int. J. Manuf. Technol. Manag. 33 (2019) 76–87.
[29] J. Damon, S. Dietrich, S. Gorantla, U. Popp, B. Okolo, V. Schulze, Process porosity and mechanical performance of fused filament fabricated 316L stainless steel, Rapid Prototyp. J. 25 (2019) 1319–1327.
[30] R. Santamaria, M. Salasi, S. Bakhtiari, G. Leadbeater, M. Iannuzzi, Z. Quadir, Microstructure and mechanical behaviour of 316L stainless steel produced using sinter-based extrusion additive manufacturing, J. Mater. Sci. (2021).
[31] R. Casati, J. Lemke, M. Vedani, Microstructure and Fracture Behavior of 316L Austenitic Stainless Steel Produced by Selective Laser Melting, J. Mater. Sci. Technol. 32 (2016) 738–744.

[32] E. Liverani, S. Toschi, L. Ceschini, A. Fortunato, Effect of selective laser melting (SLM) process parameters on microstructure and mechanical properties of 316L austenitic stainless steel, J. Mater. Process. Technol. 249 (2017) 255–263.
[33] A. Yadollahi, N. Shamsaei, S.M. Thompson, D.W. Seely, Effects of process time interval and heat treatment on the mechanical and microstructural properties of direct laser deposited 316L stainless steel, Mater. Sci. Eng. A. 644 (2015) 171–183.
[34] X. Chen, J. Li, X. Cheng, B. He, H. Wang, Z. Huang, Microstructure and mechanical properties of the austenitic stainless steel 316L fabricated by gas metal arc additive manufacturing, Mater. Sci. Eng. A. 703 (2017) 567–577.
[35] A276/A276M-17 Standard Specification for Stainless Steel Bars and Shapes, ASTM International, 2017.
[36] N. Kurgan, Effect of porosity and density on the mechanical and microstructural properties of sintered 316L stainless steel implant materials, J. Mater. 55 (2014) 235–241.
[37] P. V. Muterlle, M. Zendron, M. Perina, A. Molinari, Influence of delta ferrite on mechanical properties of stainless steel produced by MIM, 20th Int. Congr. Mech. Eng. (2009) 1–6.
[38] T. Ronneberg, C.M. Davies, P.A. Hooper, Revealing relationships between porosity , microstructure and mechanical properties of laser powder bed fusion 316L stainless steel through heat treatment, Mater. Des. 189 (2020) 108481.
[39] L. Liu, N. Loh, B. Tay, Constitutive modelling of sintering of 316L stainless steel microsize structures, Appl. Mech. Mater. 149 (2012) 846–851.
[40] J. Li, C. Yuan, J. Guo, J. Hou, L. Zhou, Effect of hot isostatic pressing on microstructure of cast gas-turbine vanes of K452 alloy, Prog. Nat. Sci. Mater. Int. 24 (2014) 631–636.
[41] B. Dzepina, D. Balint, D. Dini, A phase fi eld model of pressure-assisted sintering, J. Eur. Ceram. Soc. 39 (2019) 173–182.
[42] S.L. Taylor, R.N. Shah, D.C. Dunand, Ni-Mn-Ga micro-trusses via sintering of 3D-printed inks containing elemental powders, Elsevier B.V., 2018.
[43] A. Mostafaei, C. Hilla, E.L. Stevens, P. Nandwana, A.M. Elliott, M. Chmielus, Comparison of characterization methods for differently atomized nickel-based alloy 625 powders, Powder Technol. 333 (2018) 180–192.
[44] D. Kianersi, A. Mostafaei, A.A. Amadeh, Resistance spot welding joints of AISI 316L austenitic stainless steel sheets: Phase transformations, mechanical properties and microstructure characterizations, Mater. Des. 61 (2014) 251–263.
[45] M. Hajian, A. Abdollah-zadeh, S.S. Rezaei-nejad, H. Assadi, S.M.M. Hadavi, K. Chung, Microstructure and mechanical properties of friction stir processed AISI 316L stainless steel, J. Mater. 67 (2015) 82–94.
[46] F. Mirakhorli, F.M. Ghaini, M.J. Torkamany, Þ. Eq, Development of Weld Metal Microstructures in Pulsed Laser Welding of Duplex Stainless Steel, 21 (2012) 2173–2176.
[47] D.M. Xu, G.Q. Li, X.L. Wan, R.L. Xiong, G. Xu, K.M. Wu, M.C. Somani, R.D.K. Misra, Materials Science & Engineering A Deformation behavior of high yield strength – High ductility ultra fine- grained 316LN austenitic stainless steel, 688 (2017) 407–415.
[48] J. Suryawanshi, K.G. Prashanth, U. Ramamurty, Mechanical behavior of selective laser melted 316L stainless steel, Mater. Sci. Eng. A. 696 (2017) 113–121.
[49] A.J. Cooper, W.J. Brayshaw, A.H. Sherry, Tensile Fracture Behavior of 316L Austenitic

Stainless Steel Manufactured by Hot Isostatic Pressing, Metall. Mater. Trans. A. 49 (2018) 1579–1591.
[50] E. Ryshkewitch, Compression Strength of Porous Sintered Alumina and Zirconia, J. Am. Ceram. Soc. 36 (1953) 65–68.
[51] F. Ternero, P. Urban, J.M. Montes, Influence of the Total Porosity on the Properties of Sintered Materials — A Review, (2021).
[52] S.A.E. International, S.A.E. Transactions, The Influences of Porosity on the Characteristics of Sintered Materials, 95 (1986) 790–805.
[53] L.I.U.P. Nz, F.U. Chao, Relationship between tensile strength and porosity for high porosity metals, 42 (1998).
[54] K.K. Singh, Strain hardening behaviour of 316L austenitic stainless steel, Mater. Sci. Technol. 20 (2004) 1134–1142.
[55] D.C. Ludwigson, Modified stress-strain relation for FCC metals and alloys, Metall. Trans. 2 (1971) 2825–2828.
[56] S. Hertelé, W. De Waele, R. Denys, A generic stressstrain model for metallic materials with two-stage strain hardening behaviour, Int. J. Non. Linear. Mech. 46 (2011) 519–531.
[57] T.J. Headley, J.A. Brooks, A New Bcc-Fcc Orientation Relationship Observed between Ferrite and Austenite in Solidification Structures of Steels, 33 (2002) 5–15.
[58] C. Örnek, D.L. Ngelberg, An experimental investigation into strain and stress partitioning of duplex stainless steel using digital image correlation , X-ray diffraction and scanning Kelvin probe force microscopy, 51 (2016) 207–219.
[59] S. Kibey, J.B. Liu, D.D. Johnson, H. Sehitoglu, Predicting twinning stress in fcc metals: Linking twin-energy pathways to twin nucleation, Acta Mater. 55 (2007) 6843–6851.
[60] D.G. Brandon, The structure of high-angle grain boundaries, Acta Metall. 14 (1966) 1479–1484.
[61] M.A. Meyers, L.E. Murr, A model for the formation of annealing twins in F.C.C. metals and alloys, Acta Metall. 26 (1978) 951–962.